Unveiling the Selenization Reaction Mechanisms in Ambient Air-Processed Highly Efficient Kesterite Solar Cells

Zixuan Yu, Chuanhao Li, Shuo Chen, Zhuanghao Zheng, Ping Fan, Yingfen Li, Manlin Tan, Chang Yan, Xianghua Zhang, Zhenghua Su, et al.

Unveiling the Selenization Reaction Mechanisms in Ambient Air-processed Highly Efficient Kesterite Solar Cells

Zixuan Yu,Chuanhao Li, Shuo Chen, Zhuanghao Zheng, Ping Fan, Yingfen Li, Manlin Tan, Chang Yan, Xianghua Zhang,Zhenghua Su, and Guangxing Liang**

Z. Yu, C. Li, S. Chen, Z. Zheng, P. Fan, Z. Su, G. Liang
Shenzhen Key Laboratory of Advanced Thin Films and Applications, Key Laboratory of Optoelectronic Devices and Systems of Ministry of Education and Guangdong Province, College of Physics and Optoelectronic Engineering,
Shenzhen University
Shenzhen, 518060, China
E-mail: lgx@szu.edu.cn (Prof. Liang) and zhsu@szu.edu.cn (Prof. Su)
Y. Li
College of Materials and Energy Engineering, Guizhou Institute of Technology, Guiyang, 550003, China
M. Tan
Research Institute of Tsinghua University in Shenzhen, Shenzhen 518055, China
C. Yan
Sustainable Energy and Environment Thrust, Jiangmen Laboratory of Carbon Science and Technology, The Hong Kong University of Science and Technology (Guangzhou), Guangzhou, 510000, China
X. Zhang
CNRS, ISCR (Institut des Sciences Chimiques de Rennes), UMR 6226,
Université de Rennes
Rennes F-35000, France

Keywords: Kesterite; Selenization; Solar cells; Efficiency

Abstract: The selenization annealing process is vital for highly efficient kesterite solar cells. Adding SnS during annealing proves to be effective. Nevertheless, massive S element is also introduced under the condition of sufficient Sn element supplement by SnS, which inevitably leads to plenty of defects. Meanwhile, the path of supplementing Sn is never elucidated. Herein, to play the role of SnS and avoid introducing excess S, the combination strategies of SnS and Sn or SnSe or $SnSe_2$ are first put forward. And the composition of the vapor inhibiting Sn loss (gaseous $SnSe_3$) and pathway that $SnSe_3$ facilitates the formation of CZTSSe are first clarified. When $SnSe_2$ is added to SnS in the selenization process, grain fusion is effectively promoted. The high crystalline quality kesterite absorber makes the band bending at the GBs optimal and the interface recombination be effectively suppressed. Moreover, cation disorders are remarkably reduced. Therefore, the V_{oc} is significantly elevated from 508 mV to 546 mV with increased FF and J_{sc}. Eventually, state-of-the-art ambient air-processed kesterite device with 12.89% efficiency is achieved, and the unveiled reaction mechanisms have guiding significance for further optimizing selenization atmosphere and elevating the efficiency of CZTSSe solar cells.

1. Introduction

What is noteworthy is that high-efficiency thin film solar cells play a vital role in realizing building integrated photovoltaics (BIPV). Among numerous potential photovoltaic materials, kesterite semiconductor $Cu_2ZnSn(S_xSe_{1-x})_4$ (CZTSSe) is a promising thin-film photovoltaic material due to its similar crystalline structure as chalcopyrite $Cu(In_xGa_{1-x})Se_2$ (CIGS) and earth-abundant elements. The solution preparation methods of CZTSSe absorber have been extensive researched since IBM achieved world-record 12.6% efficiency CZTSSe thin-film solar cell by hydrazine pure-solution approach in 2014.[1] As we all know, hydrazine is highly toxic and dangerous, so a variety of environmentally friendly solvent systems have been developed to replace hydrazine solvent over the years, like dimethyl sulfoxide (DMSO),[2] dimethyl formamide (DMF),[3] 2-Methoxyethanol,[4] and amine-thiol.[5]

Recently, Gong et al. achieved a new world record of 12.96% efficiency by using DMSO solvent,[6] which brings a new dawn to CZTSSe solar cells, especially CZTSSe solar cells prepared by solution methods. Although the progress is encouraging, the highest efficiency of CZTSSe solar cells is still far below its theoretical value and the efficiency record of CIGS (23.35%),[7] which is mainly attributed to the large open-circuit voltage deficit ($V_{oc,def}$). How to minimize the $V_{oc,def}$ is a priority for the further efficiency improvement of CZTSSe solar cells. The $V_{oc,def}$ can be calculated by V_{OC}^{SQ}-V_{OC}, where V_{OC}^{SQ} is the maximum achievable open-circuit voltage (V_{oc}) based on the Shockley–Queisser limit. And V_{OC}^{SQ} can be obtained by $0.9324E_g$-0.1666, where E_g is the bandgap of the absorber.[2] One of the advantages of CZTSSe is the tunable band gap, and the schemes via adjusting the proportion or distribution of cation or anion are often implemented to tune the band gap or construct the gradient band gap and thus lift the V_{oc}. In the field of CIGS solar cells, highly efficient CIGS solar cells with the gradient band gap were achieved by modifying Ga gradient. [7-8] For CZTSSe solar cells, the theoretical calculation shows that the composition-graded $(Cu_{1-x}Ag_x)_2ZnSn(S,Se)_4$ alloys with a p-to-n type inversion should be ideal light-absorber materials because of a large band bending from the interior of the absorber to the junction interface. The degree of band bending determines the value of the V_{oc}. The greater the band bending, the larger the V_{oc}.[9] Meanwhile, more and more experiments have proved that the incorporation of Ag^+ into kesterite is an effective strategy for achieving higher efficiency solar cells.[10-13] Based on the merits of Ag^+, Ag^+ was also incorporated into our CZTS precursor solution from the mixture of Sn^{4+} ($SnCl_4 \cdot 5H_2O$) and Sn^{2+} ($SnCl_2 \cdot 2H_2O$) precursor solution with a 1:1 ratio, and the efficiency was increased from 11.02% to 11.60% as expected, but 11.60% was not the end.

In addition to the optimization of the precursor solution, the selenization annealing process is also critical for the grain growth of absorber, which is a crucial step in the transition from CZTS precursor phase and massive secondary phases to kesterite CZTSSe. And the selenization atmosphere is particularly important for the process of

phase evolution among many influencing factors of selenization process. For example, S (Sulfur) and Se (Selenium) powder were often utilized to adjust S and Se content during annealing treatment to obtain different S/Se ratios.[14-17] But the S/Se ratio is difficult to control precisely because of the huge discrepancy in the activity of S and Se. In particular, S powder is easily evaporated on account of its low melting point, low boiling point and high saturated vapor pressure, resulting in excessive content of S or uneven distribution of S and Se in the films, which are more prone to produce massive defects in the absorbers. Compared to S powder, S is less active in the compounds, so many research groups applied S compounds such as SeS_2, H_2S, and SnS in the selenization process to control the S/Se ratio more accurately.[18-21] However, SnS also showed the prominent advantage in suppressing Sn (Tin) loss by supplementing Sn-contained vapor and thus better crystalline quality absorbers, except that the band gap of absorber could be tuned flexibly and the thickness of $Mo(S,Se)_2$ layer could be significantly reduced by providing S_2 vapor.[20-23] Actually, what the Sn-contained vapor is and how it is involved in promoting the formation of CZTSSe have not been clearly clarified yet. At the same time, with the introduction of SnS, S content is also increased under the condition of sufficient Sn supplement. Although the V_{oc} can be elevated by enlarging the band gap of the absorber with increased S content, there is a serious but not negligible problem that plenty of defects will be introduced, which is significantly detrimental to the device performance.[17, 24]

Herein, Sn, SnSe and $SnSe_2$ were added respectively in the selenization process based on SnS and Se under the condition that the molar quantity of Sn remains unchanged, that is, the selenization conditions (SnS+Sn+Se, SnS+SnSe+Se, and SnS+$SnSe_2$+Se). And the other six selenization ingredients (Se, Sn+Se, SnSe+Se, $SnSe_2$+Se, SnS+Se, SnS_2+Se) were also tried in order to clarify the reaction and promotion mechanisms. By analyzing the composition of residual powders and thin films, the constituent of the vapor inhibiting Sn loss (gaseous $SnSe_3$) and pathway that $SnSe_3$ facilitates the formation of CZTSSe are first clarified. When $SnSe_2$ was added to SnS in the selenization process, grain fusion was effectively promoted. Eventually, a champion

kesterite solar cell with 12.89% efficiency under the condition ($SnS+SnSe_2+Se$) was achieved, which was the highest efficiency for ambient air-processed CZTSSe solar cells. In addition, the V_{oc} was greatly lifted from 508 mV to 546 mV with increased FF and J_{sc}. The $V_{oc,def}$ of 350 mV and V_{OC}/V_{oc}^{SQ} of 60.91% were not only the best among the above conditions but also the optimum for CZTSSe solar cells based on air-processed precursors, and were at the forefront of high efficiency cells of other solvent systems.

2. Results and Discussion

2.1. Determination of Products and Reaction Paths

Based on the previous precursor solution scheme, that is, Sn^{4+} and Sn^{2+} precursor solutions were mixed with a 1:1 ratio as final precursor solution,[25] Ag^+ doping strategy was also adopted. Detailed operation procedure was shown in **Figure S1**. The efficiencies of solar cells with different Ag ratios ($\frac{n(Ag)}{n(Ag)+n(Cu)}$=0%, 2%, 3%, 4%, 5%, 6%, 7%, 8%, 11%) were presented in **Figure S2**. Obviously, this group of efficiency boxes shows the shape of a mountain peak, and the 5% Ag ratio was at the top. In terms of the maximum efficiency, the incorporation of 2%~7% Ag all can promote the efficiency. Consequently, compared to the reference sample, the efficiency was increased from 11.02% to 11.60% with 5% Ag, and the other three parameters were all improved. (**Figure S3** and **Table S1**) Next, nine selenization ingredients (Se, Sn+Se, SnSe+Se, $SnSe_2$+Se, SnS+Sn+Se, SnS+SnSe+Se, SnS+$SnSe_2$+Se, SnS+Se, SnS_2+Se) based on high Se content were systematically investigated. “Se” means the selenization ingredient is only Se granules; “X+Se” means the selenization ingredients are the combination of different powders and Se granules. For example, “SnS+$SnSe_2$+Se” represents the combination of the evenly mixed SnS and $SnSe_2$ powders and Se granules. To be more concise, the above nine selenization ingredients are represented by the letters A~I, respectively. Taking the selenization condition ($SnS+SnSe_2+Se$) as an example, the thin film is defined as film-G and the device is defined as device-G in the main body and the legends of all the figures and tables.

In order to determine the influence of nine selenization ingredients in the selenization process and clarify the mechanism of inhibiting Sn loss, it is necessary to analyze and

confirm the composition of the residuary products after annealing, first of all, X-ray diffraction (XRD) patterns and Raman spectra of the residuary powders were presented in **Figure 1**a, b. The residuary powders under all conditions exhibited the same number of diffraction peaks and similar peak positions in XRD patterns, implying that the products from different ingredients may be the same phase. In general, Sn and SnSe react with Se respectively at high temperatures according to the following equations: [20, 26]

$$Sn + Se_2 \rightarrow SnSe_2 \quad (1)$$

$$2SnSe + Se_2 \rightarrow 2SnSe_2 \quad (2)$$

Thus, $SnSe_2$ as product was considered first. It was found that the diffraction peaks fit well with the standard card $SnSe_2$ PDF#23-0602 apart from (100) diffraction peak regardless of peak shift. After reviewing the literature, (100) diffraction peak was still attributed to $SnSe_2$ phase regardless of peak shift.[26] In fact, there were peak shifts to larger angles relative to the standard card of $SnSe_2$ under all conditions and the peak shifts can not be ignored. Since the ionic radius of S is smaller than that of Se, when Se atom is replaced by S atom, the diffraction peak will shift to larger angles. Therefore, it can be determined that the final powder products are intermediate phase $SnSe_{2(1-x)}S_{2x}$ between $SnSe_2$ and SnS_2 under all conditions. And under the conditions of B, C and D, the intermediate phase $SnSe_{2(1-x)}S_{2x}$ come from the substitution reaction between $SnSe_2$ and S_2. The substitution equation is as follows:

$$SnSe_2 + S_2 \rightarrow SnSe_{2(1-x)}S_{2x} \quad (3)$$

In the above equation, S_2 vapor may come from the decomposition of CZTS. The equation is as follows:[27-30]

$$Cu_2ZnSnS_4(s) \rightleftharpoons Cu_2S(s) + ZnS(s) + SnS(s,g) + \frac{1}{2}S_2(g) \quad (4)$$

Next, the standard card SnS_2 PDF#83-1707 was employed. Clearly, the diffraction peaks of the residuary powders were indeed located between the peaks of the standard $SnSe_2$ and SnS_2 phases, which was evident from the enlarged (101) diffraction peak (Figure 1a, right), and (101) peak was analyzed in detail here. If these eight residuary

powders were divided into four groups according to S content of selenization ingredients (the first group: B, C and D; the second group: E, F and G; the third group: H; the fourth group: I), it is obvious that the degrees of 2θ of (101) peak became larger as the S content increases among these four groups. But within the first group and the second group, there were also peak shifts. The degrees of 2θ of (101) peak were presented in **Table S2** and the comparative results about the degrees of 2θ were that B ＜C＜D and E＜F＜G. The results are surprisingly consistent in these two groups. According to the literature,[31] Shimada et al. confirmed that $SnSe_2$ and SnSe follow decomposition **Equation 5** and **6** at high temperature:

$$2SnSe_2 \rightleftharpoons 2SnSe + Se_2(g) \quad \text{(Starting temp: 340 °C)} \tag{5}$$

$$3SnSe \rightleftharpoons 2Sn + SnSe_3(g) \quad \text{(Starting temp: Above 400 °C)} \tag{6}$$

So, for selenization ingredients containing $SnSe_2$, $SnSe_2$ starts to decompose as soon as the selenization temperature reaches 340 °C, but Sn and SnSe need react with Se first to form $SnSe_2$ in the selenization process and then $SnSe_2$ decomposes. Thus, there was more $SnSe_2$ left in the residuary powders of B, C, E and F to make their diffraction peaks closer to that of $SnSe_2$. For the reason why the degrees of 2θ of B (E) was smaller than those of C (F), firstly, part of SnSe will decompose when the temperature reaches 400 °C. Secondly, the reaction rate of Sn and Se may be slower than that of SnSe and Se so that less $SnSe_2$ was decomposed. Raman spectrum was further carried out, which is a kind of scattering spectrum that can get the information about molecular vibration and rotation. As shown in Figure 1b, the Raman peaks of A_{1g} mode of $SnSe_2$ show the similar peak shift trend as XRD patterns, and the reason for this trend is the same as explained above. As the lattice constant of SnS_2 (3.70 Å) is smaller than that of $SnSe_2$ (3.87 Å), there was observed red shift for the A_{1g} mode of $SnSe_2$ with increased S content of the selenization ingredients, indicating that more S was substituted for Se. [32] Thus, the residuary powders were again proved to be intermediate phase $SnSe_{2(1-x)}S_{2x}$ by Raman spectroscopy measurement. To our knowledge, the Raman spectra of $SnSe_{2(1-x)}S_{2x}$ ($0 \leq x \leq 1$) show a two-mode behavior with local and gap modes. There are E_g and A_{1g} modes belonging to Raman active modes and coming from the dominant

contribution of the exciton in $SnSe_2$ and SnS_2.[33-34] In theory, the Raman peaks of the E_g and A_{1g} modes of $SnSe_2$ are located at 107.9 cm^{-1} and 187.0 cm^{-1} and those of SnS_2 are at 194.6 cm^{-1} and 322.6 cm^{-1} respectively.[35] Actually, their positions are affected by preparation methods[32, 36-37] and composition in the mixed crystals, like $SnSe_{2(1-x)}S_{2x}$, $Mo_{1-x}W_xS_2$, $WS_{2(1-x)}Se_{2x}$.[32, 38-39] We note that the Raman spectra of B, C, D, E, F, G, H these conditions all only had two Raman peaks, while I owned three Raman peaks. The values of all peak positions were showed in **Table S3**. According to the literature,[33] these two Raman peaks of the former were assigned to the E_g and A_{1g} modes of $SnSe_2$ respectively and $0 \leq x \leq 0.125$ of $SnSe_{2(1-x)}S_{2x}$ can be concluded. For I, the Raman peaks at 123.13 cm^{-1} and 298.22 cm^{-1} were the E_g mode of $SnSe_2$ and the A_{1g} mode of SnS_2 respectively. And the Raman peak at 198.72 cm^{-1} may be the superposition of the peak of A_{1g} mode of $SnSe_2$ and that of E_g mode of SnS_2 in that these two peaks are very close to each other in theory and the peak was much wider. The value of x for $SnSe_{2(1-x)}S_{2x}$ under the condition of I may be $0.3125 \leq x \leq 0.5$. Moreover, for the conditions of E, F, G, H, I, the formation of S_2 vapor except $SnSe_{2(1-x)}S_{2x}$ need further confirmation via XRD and Raman results of thin films.

Therefore, XRD patterns and Raman spectra of absorbers were analyzed (Figure 1c, d**).** The XRD and Raman peak shift trends of the films were neither the same nor opposite to that of the residuary powders but showed their own laws. As shown in Figure 1c, all diffraction peaks were located between the peaks of the standard kesterite $Cu_2ZnSnSe_4$ (PDF#52-0868) and Cu_2ZnSnS_4 phases (PDF#26-0575) and no diffraction peaks of the secondary phases were observed, indicating that pure kesterite phase was obtained under all conditions. In theory, the band gaps of pure CZTSe and CZTS is 1.0 eV and 1.5 eV respectively but the band gap of $(Cu_{1-y}Ag_y)_2ZnSn(S_xSe_{1-x})_4$ depends on the values of x and y; that is, when x or y increases, the band gap of $(Cu_{1-y}Ag_y)_2ZnSn(S_xSe_{1-x})_4$ will enlarge.[13, 20] Since the same amount of Ag solution (5% Ag) was added to the precursor solutions, the band gaps of our devices were only determined by the value of x. For this reason, the positions of diffraction peaks only depend on x (S and Se content), so it is directly related to the band gap. The magnification figure of (112) diffraction

peak was shown on the right of Figure 1c and the degrees of 2θ of it were presented in **Table S4**. According to the position of (112) diffraction peak, the nine CAZTSSe films can be divided into four groups (the first group: A, B, C and D; the second group: E; the third group: F, G and H; the fourth group: I). They were grouped based on the fact that if (112) diffraction peaks were at the same location, they would be grouped into the same group. Being in the same group means that the band gaps of the devices were the same. At the same time, the positions of Raman peak for the A_1 mode of CAZTSSe (Figure 1d and **Table S5**) show the same law as those of (112) diffraction peaks, so such a grouping rule is reliable. The shift of the diffraction peaks to larger angles in XRD and the red shift of Raman peaks in Raman from the first group to the fourth group both mean that the band gap gradually became larger, indicating that S successfully incorporated into CAZTSSe bulk. Therefore, S_2 vapor was indeed produced except $SnSe_{2(1-x)}S_{2x}$ in the selenization process under the conditions of E, F, G, H and I. Combining the results of XRD patterns and Raman spectra of the powders and films, the equations under these conditions are as follows:

$$SnS + Sn + Se_2 \rightarrow SnSe_{2(1-x)}S_{2x} + S_2(g) \quad (7)$$

$$SnS + SnSe + Se_2 \rightarrow SnSe_{2(1-x)}S_{2x} + S_2(g) \quad (8)$$

$$SnS + SnSe_2 + Se_2 \rightarrow SnSe_{2(1-x)}S_{2x} + S_2(g) \quad (9)$$

$$SnS + Se_2 \rightarrow SnSe_{2(1-x)}S_{2x} + S_2(g) \quad (10)$$

$$SnS_2 + Se_2 \rightarrow SnSe_{2(1-x)}S_{2x} + S_2(g) \quad (11)$$

S_2 vapor plays an important role in enhancing the V_{oc} by participating in the formation of CAZTSSe to enlarge its band gap. The problem that why the band gaps of the devices were not positively correlated with S content of selenization ingredients will be discussed in detail in external quantum efficiency (EQE) section. To sum up, $SnSe_{2(1-x)}S_{2x}$ and S_2 these two products were identified. Since our precursor solution contains Sn^{2+} and Sn^{4+}, both the multi-step secondary phase fusion reaction for Sn^{2+} precursor film and direct phase transformation reaction for Sn^{4+} precursor film need to be

considered. The main selenization reaction paths given by Gong et al. are as follows:[2]

$$Cu_2S + Se_2 \rightarrow Cu_2Se \quad (12)$$

$$SnS + Se_2 \rightarrow SnSe_2 \quad (13)$$

$$ZnS + Se_2 \rightarrow ZnSe \quad (14)$$

$$Cu_2Se + SnSe_2 \rightarrow Cu_2SnSe_3 \quad (15)$$

$$Cu_2SnSe_3 + \mathrm{ZnSe} \rightarrow Cu_2ZnSnSe_4 \quad (16)$$

$$Cu_2Se + SnSe_2 + ZnSe \rightarrow Cu_2ZnSnSe_4 \quad (17)$$

$$Cu_2ZnSnS_4 + Se_2 \rightarrow Cu_2ZnSn(S,Se)_4 \quad (18)$$

And the equation of CZTSSe decomposition is as follows:[21, 27-28]

$$Cu_2ZnSnS(e)_4(s) \rightleftharpoons Cu_2S(e)(s) + ZnS(e)(s) + SnS(e)(s,g) + \frac{1}{2}S(e)_2(g) \quad (19)$$

where (s) and (g) indicate solid and gas phases respectively. For by-products Cu_2S(e), ZnS(e) and SnS(e), SnS(e) have high saturated vapor pressure in the temperature range of interest. Thus, SnS(e) exist as the solid and gas phases. The equation is as follows:

$$SnS(e)(s) \rightleftharpoons SnS(e)(g) \quad (20)$$

Gaseous SnS(e) will escape from the film surface, which is the reason of Sn loss and will accelerate the decomposition of CZTSSe. Meanwhile, compared with Cu_2S(e) and ZnS(e), $SnSe_2$ and SnS(e) is more unstable because breaking Sn-S or Sn-Se bonds is easier in the compounds.[40] From the above equations, by supplementing $SnSe_2$ in **Equation 15** and **17** and SnS(e) in **Equation 19**, the production of CZTSSe can be promoted and the decomposition of CZTSSe can be inhibited. As far as we know, $SnSe_2$, SnSe, and SnS all have high melting points, well above the selenization temperature (555 °C), which make it difficult for them to provide Sn-contained vapor through evaporation, so sublimation and thermal decomposition were considered. The thermal decomposition equations of $SnSe_2$ and SnSe were shown in Equation 5 and 6 and those of SnS_2 and SnS were shown below:[31]

$$2SnS_2 \rightleftharpoons 2SnS + S_2(g) \quad \text{(Starting temp: 550 °C)} \quad (21)$$

$$3SnS \rightleftharpoons 2Sn + SnS_3(g) \quad \text{(Starting temp: 740 °C)} \quad (22)$$

Since our selenization temperature was only 555 °C, the decomposition of SnS was not considered. Although the saturated vapor pressure of SnSe at 550 °C is relatively high,

there was very little sublimation of $SnSe_2$ and SnSe because the selenization process was carried out at about 1 atm. Meanwhile, the decomposition temperature of $SnSe_2$ (340 °C) and SnSe (above 400 °C) is much lower than the selenization temperature (555 °C), so $SnSe_2$ and SnSe were mainly decomposed during selenization. On the other hand, the diffraction peaks of intermediate phase $SnSe_{2(1-x)}S_{2x}$ were very close to that of $SnSe_2$ phase by XRD, so very few amounts of SnS were supplied via its decomposition. In conclusion, it can be determined that the composition of the Sn-contained vapor inhibiting Sn loss and promoting CZTSSe production during selenization was almost all gaseous $SnSe_3$ from the decomposition of SnSe and $SnSe_2$. The gaseous $SnSe_3$ was indirectly involved in Equation 15, 17 and 19 by suppressing the decomposition of SnSe and $SnSe_2$ to promote the production of CZTSSe and inhibit the decomposition of CZTSSe. To sum up, the constituent of the Sn-contained vapor (gaseous $SnSe_3$) and pathway that $SnSe_3$ facilitates the formation of CZTSSe are first proposed. And S_2 vapor was also involved in Equation 19 to inhibit the decomposition of CZTSSe and thus S incorporated into CZTSSe bulk to lift the V_{oc} by enlarging the band gap. The reaction mechanism of inhibiting Sn loss and supplementing S in the selenization process was presented in **Scheme 1**, and more detailed mechanism of efficiency promotion will be clearly illustrated in SEM part combined with the above equations.

As shown in Figure 1d, there are three scattering peaks of the B, A_1, and E vibration modes of CAZTSSe and the members of the first group showed stronger peak intensity especially for the scattering peak of A_1 mode. As far as we know, the A_1 mode originates from the vibration of Se atoms surrounded by other atoms in the lattice,[25] indicating an increase of Se content in these absorbers compared with the films under other conditions. As can be seen from the enlarged Raman peak of A_1 mode (Figure 1d, right), there were red shifts from the first group to the fourth group. Besides, the scattering peak of A vibration mode of CAZTS exists the second, third and fourth group, which is attributed to the vibration of S atoms.[25] The intensity of this peak is directly proportional to S content in the films. For example, this Raman peak shows the

strongest intensity under the condition of I, indicating that the most S incorporated into CAZTSSe bulk. The results of XRD patterns and Raman spectra of CAZTSSe films both demonstrate that there were no redundant secondary phases under all selenization conditions. At last, as in the case of $SnSe_{2(1-x)}S_{2x}$, the reason why the diffraction peaks shifted toward larger angles in XRD patterns when Se atoms were replaced by S atoms in CZTSSe lattice is that the ionic radius of S is smaller than that of Se. For Raman spectra, the reason of the red shift when the heavier Se atoms were replaced by the lighter S atoms is that the Raman shift is inversely proportional to the mass of atoms.

2.2. Effects of Selenization Atmosphere on Grain Growth

As shown in **Figure 2** and **Figure S4**, the surface and cross-section morphology by scanning electron microscope (SEM) of CAZTSSe films under the nine selenization ingredients (A~I) based on high Se content were systematically investigated to study the effects of different selenization atmospheres on grain growth and then the efficiencies of the devices. The statistical distribution of the device photovoltaic parameters under these nine selenization ingredients were presented in **Figure S5**.

For the film surfaces under the nine selenization atmospheres, the morphology of the films under the conditions of H and I looked alike and that of the films under the remaining conditions (A, B, C, D, E, F, G) showed similarity. To be specific, the grains of the former appeared more angular and that of the latter were much rounder. This phenomenon demonstrates that when the selenization atmosphere contains much S, the film will exhibit similar surface morphology as shown in Figure 2a and Figure S4d. Moreover, the grain size of film-I was significantly smaller than that of film-H, which indicates that too much S was not conducive to grain growth. This is also evidenced by the fact that the grains under other conditions all showed larger grain sizes than the grains under the condition of I. Compared with the surface morphology of film-A and D, film-B and C had obvious holes but not in the former. The causes of this phenomenon were analyzed carefully. For the conditions of A and D, Se_2 atmosphere coming from Se granules all directly served the formation of CZTSSe mainly via **Equation 12~14** and 19. And gaseous $SnSe_3$ from the decomposition of $SnSe_2$ was indirectly involved

in Equation 15, 17 and 19 to promote the production of CZTSSe and inhibit the decomposition of CZTSSe. Nevertheless, for the condition of C, although part of SnSe will decompose to produce $SnSe_3$ when the temperature reaches 400 °C, part of SnSe need react with Se_2 to form $SnSe_2$. For the condition of B, whole Sn need react with Se_2 to form $SnSe_2$ first and then $SnSe_2$ decomposes. It means that in the above two conditions, most of Se_2 atmosphere was used for **Equation 1** and **2** initially, leading to the delay in the growth of CZTSSe top grains and thus the formation of holes, which is why the promoting effects of Sn and SnSe on grain growth were not as significant as those of $SnSe_2$ and were worse than those of only Se in the case of $SnSe_3$ gas. After Sn, SnSe and $SnSe_2$ was added to SnS respectively, the films presented denser morphology and the holes were significantly reduced. This shows under 1:2 mole ratio of SnS:Sn, SnS:SnSe and SnS:$SnSe_2$, SnS played a critical role in regulating the reaction rate and supplementing S content in the films, and thus the grain growth and the corresponding efficiencies were promoted. Also, film-G consisted of the largest and densest grains. In summary, the surface quality of CAZTSSe films was the best under the condition of G, which is necessary for the construction of superior P-N junction and the reduction of interface defects.

Surprisingly, an intriguing phenomenon was found in the cross-sectional SEM images that compared with the middle fine-grained layers of the tri-layer sandwich structure of film-H and film-I, the middle fine-grained layer all grew up under the conditions of B, C and D. After Sn, SnSe and $SnSe_2$ was added to SnS respectively, another intriguing phenomenon that the top large grains merged with the middle grains to construct a macrocrystalline layer emerged. Compared with the conditions of H and I, the cross sections under the conditions of E, F and G had distinct results although their products were the same according to **Equation 7~11**. And it is clear that the cross-sectional morphology of film-G was the best as its grains were most tightly bonded among film-E, F and G. This not only reduced grain boundaries but also made element distribution more uniform as verified by scanning transmission electron microscopy (STEM). The reason why the cross-sectional morphology of film-G was optimal among the above

three conditions can be ascribed to the most appropriate growth rate of different grain layers of absorber resulting from the most suitable supply rate of S_2 vapor and gaseous $SnSe_3$ at this point, which effectively promoted the grain fusion of different layers.[41] Furthermore, the reasons for the difference in $MoSe_2$ thickness between film-H, D and G were analyzed in depth. The literature suggests that S has stronger affinity than Se to molybdenum, and thus the formation of MoS_2 is easier than $MoSe_2$, which results in the suppressed formation of $MoSe_2$ layer from the competition reaction between S and Se with molybdenum.[20] So, the more S content in the selenization atmosphere, the thinner the thickness of $MoSe_2$. Compared to film-H and G, the thickness of $MoSe_2$ of film-D increased because of no additional supply of S for the condition of D. Whereas, although the S content of G was less than that of H, the thickness of $MoSe_2$ of film-G decreased, which was the dual action of SnS and $SnSe_2$ under the condition of G. On the one hand, SnS attracted some Se_2 vapor to react with it in the selenization process and then produced S_2 vapor to participate in Equation 19. On the other hand, more Se_2 vapor was utilized to promote the production of CZTSSe and inhibit the decomposition of CZTSSe with the help of gaseous $SnSe_3$ from the decomposition of $SnSe_2$. Combining the above two points, they mean that more Se_2 vapor was consumed for the generation of CZTSSe under the condition of G, so the formation of $MoSe_2$ was effectively inhibited because of the lack of Se_2 vapor to react with the molybdenum and thus the series resistance was reduced as shown in **Table 1**. According to the above analyses, the densest macrocrystalline absorber with the largest grains and the thinnest $MoSe_2$ of film-G show the superiority of the combination of SnS and $SnSe_2$, much better than they work alone, indicating that gaseous $SnSe_3$ combined with few amounts of S_2 vapor had the best effect on grain growth, as shown in Figure 2i. Accordingly, the devices under the condition of G show great advantages in V_{OC} and FF, and thus the best efficiencies were obtained (Figure S5). Besides, the results of the surface and cross-section morphology both demonstrate that the direct supply of $SnSe_2$ is more effective than indirect supply of $SnSe_2$ through Equation 1 and 2.

2.3. Electrical Characteristics of film-H, G, and D

Subsequently, to clarify the mechanism of the efficiency improvement of G further, the electrical properties of the films and devices under the conditions of H(SnS+Se), G(SnS+$SnSe_2$+Se), and D($SnSe_2$+Se) were studied in depth except the above morphology evolution of absorber. Above all, Kelvin Probe Force Microscopy (KPFM) that is used to detect changes in the electrostatic force between the probe and sample caused by local changes in surface potential was implemented. The surface topography and contact potential difference (CPD) mapping were presented in **Figure 3**a~c and d~f respectively. The surface morphology of the three samples matched well with that shown in SEM images. The color contrast in the CPD maps represents the different values of CPD obtained from KPFM signals. We can find that the brightness at the grain boundaries (GBs) was significantly brighter than that in the grain internals (GIs) for most regions in the three samples and the brightness at the GBs gradually became brighter from Figure 3d to 3e to 3f, which indicates the change of the potential difference between the GBs and the GIs. In theory, when the voltage bias is applied to the sample during the test, the surface potential of the sample can be calculated by the following equation:

$$\varphi_2 = \varphi_1 - eV_{CPD} \tag{23}$$

when the voltage bias is applied to the probe, the surface potential can be calculated by **Equation 24**:

$$\varphi_2 = \varphi_1 + eV_{CPD} \tag{24}$$

where φ_1 is the potential of the probe, and φ_2 is the potential of the sample.[42] The voltage bias was applied to our samples here, so the surface potential was calculated by **Equation 23**. The line profiles of the surface topography and CPD mapping were shown in Figure 3g~i. According to Equation 23, the potential difference between the GIs and GBs can be expressed by the following equation:

$$\varphi_{GI} - \varphi_{GB} = eV_{CPD(GB)} - eV_{CPD(GI)} \tag{25}$$

where φ_{GI} is the potential of the GIs, and φ_{GB} is the potential of the GBs. It is obvious that the CPD at the GBs was greater than that in the GIs, so the potential at the GBs was less than that in the GIs, resulting in the downward band bending at the GBs to

attract the electrons and repel the holes. This behavior facilitated the separation of electron and hole. [43-44] In addition, the average potential difference (averaging after removing the maximum and minimum) between the GBs and GIs ($\varphi_{GI} - \varphi_{GB}$) was approximately 30 mV, 40 mV and 55 mV respectively under the conditions of H, G, and D, which indicates that the degree of the band bending at the GBs was greater and greater from H to G to D. The corresponding schematic band diagrams were shown in Figure 3j~l. To some extent, the larger the band bending at the GBs is, the more favorable it is for the separation and collection of electrons and holes. [12, 43-44] The J_{sc} was 35.14, 35.86, 38.14 mA cm^{-2} respectively under the three conditions from Table 1. Therefore, it can be inferred that this is another reason for the high J_{sc} apart from reduced band gap under the condition of D (without supplemental S). But for the devices under the condition of G, there was a significant advantage in the V_{oc} (Figure S5). In fact, the degree of band bending at the GBs should not be too large because the electrons will be easily trapped by the defects at the GBs, leading to severe carrier recombination.[45] Based on this, it is concluded that the appropriate bending of the energy band is one of the reasons for the increased V_{oc} under the condition of G.

2.4. Electrical Characteristics of device-H, G, and D

The *J-V* curves of the best devices and the statistical distribution of the device photovoltaic parameters including power conversion efficiency (PCE), open-circuit voltage (V_{OC}), fill factor (FF), and short-circuit current density (J_{SC}) under the conditions of H(SnS+Se), G(SnS+$SnSe_2$+Se), D($SnSe_2$+Se) were shown in **Figure 4**a and b. And the detailed photovoltaic parameters of the three best devices were listed in Table 1. The condition of G presents obvious advantage in V_{oc} and FF, and the best V_{oc} of 546 mV, the best FF of 67.92%, and the highest efficiency of 12.89% was achieved under the condition of G. The *J-V* curves in both forward and backward directions of the champion device show good consistency (**Figure S6**), indicating scarcely any hysteresis loss. And the benign long-term stability with slight performance degradation after 60 days was also reflected in Figure S6. Meanwhile, the Diode performance parameters of solar cells such as series resistance (R_s), shunt resistance (R_{sh}), reverse

saturation current density (J_0) and diode ideality factor (n) were calculated via CurVA software.[46-48] (Table 1 and **Figure S7**) The minimum R_s (0.83 Ω cm^2), J_0 (6.7×10^{-5} A cm^{-2}) and n (1.73) of device-G imply the reduced Shockley–Read–Hall recombination near the heterojunction and in CAZTSSe bulk. Accordingly, the thickest $MoSe_2$ layer leaded to the maximum R_s (1.38 Ω cm^2) for device-D. Moreover, the carrier transfer and recombination characteristics were also examined by Electrochemical Impedance Spectroscopy (EIS) and the relative results were shown in **Figure S8** and **Table S6**. It is worth mentioning that the series resistance (R_s'), recombination resistance (R_{rec}) and chemical capacitance (C_{rec}) here are for the equivalent circuit rather than the solar cell. And the equivalent circuit diagram was inset in the Figure S8. Likewise, the minimum R_s' (5.53 Ω) and the maximum R_{rec} (69.67 kΩ) demonstrated the improved carrier transport performance and suppressed recombination in device-G again.[49] Next, the external quantum efficiency (EQE) reflecting the optical response of the devices was further measured, presented in Figure 4c with corresponding integrated J_{SC}. The EQE of device-G exhibited a higher optical response from 390 to 500 nm, which can be attributed to the improvement of CdS functional layers.[4] In fact, the fabrication procedures of CdS layers were the same for all devices. This indicates that the improved quality of this functional layers originated from the better absorber quality that was conducive to the subsequent uniform deposition of CdS. However, the response of device-D was significantly higher in the spectral range larger than 735 nm and thus the largest integral J_{SC}. Compared with the device-H and G, the stronger spectral response from 735 to 1088 nm (E_g=1.14 eV) was attributed to the better carrier separation and collection capabilities as confirmed by KPFM, and the reduced band gap contributed to the higher spectral response in the wavelength range greater than 1088 nm. The band gaps of CAZTSSe absorber extracted from dEQE/dE were presented in Figure 4d. Apparently, the band gaps of device-H and G were the same (1.14 eV). And the band gap of device-D was 1.09 eV, less than the other two. Taking device-D, G and H as examples, the reasons why the band gaps of our devices were not positively correlated with S content of selenization ingredients were analyzed by Equation 19. For the

condition of D, there was no additional S so that the band gap of its absorber was smallest among the three conditions. However, although S content of H was more than that of G, their corresponding absorbers had the same band gaps, which meant that compared with device-G, S lost by CAZTSSe decomposition and S incorporated into CAZTSSe lattice made the final atomic ratio of S to Se of the absorber unchanged in device-H. This was a dynamic equilibrium process. The variation of the band gaps as shown in XRD patterns of the thin films for other conditions can also be analyzed from this perspective. These experimental results indicate that the selenization progress is indeed a self-regulating and self-limited process.[21, 27] Accordingly, the $V_{oc,def}$ and V_{OC}/V_{oc}^{SQ} were recorded in Table 1. Although the band gap of device-G was the same as that of device-H, an V_{oc} increment of 38 mV (508 mV to 546 mV) was obtained and thus 38 mV $V_{oc,def}$ decrement (388 mV to 350 mV). Compared to device-D, the band gap of device-G was increased from 1.09 eV to 1.14 eV and thus the V_{oc} was lifted from 477 mV to 546 mV. Even if there was a band gap increment of 50 meV, the V_{oc} was increased by 69 mV that was greater than the band gap increment with the $V_{oc,def}$ decrement of 23 mV (373 mV to 350 mV). Besides, the V_{oc} for the device-G reached 60.91% Shockley–Queisser limit (V_{OC}/V_{oc}^{SQ}). The $V_{oc,def}$ of 350 mV and V_{OC}/V_{oc}^{SQ} of 60.91% were not only the best among the three conditions but also the best for high efficiency CZTSSe solar cells based on air-processed precursors, and were at the forefront of high efficiency cells of other solvent systems. The great progress in the V_{oc} and $V_{oc,def}$ indicates that the feasibility of the combination strategy of SnS and $SnSe_2$ under high Se content. Finally, the best efficiency of 12.89% for ambient air-processed CZTSSe solar cells was achieved under the condition of G. Furthermore, the Urbach energy reflecting the band tail states of these three devices was obtained from the inverse of the slope for the linear portion below 0 in ln(-ln(1-EQE)) versus E-E_g plot. [4, 25] The values of E_u were 26.08, 25.10, 21.37 meV respectively for device-H, G, and D. The minimal E_u was for device-D, but the $V_{oc,def}$ was not the lowest at this time. When $SnSe_2$ was added to SnS, the $V_{oc,def}$ of device-G significantly decreased, which implies that the main reason for the reduction of the $V_{oc,def}$ was not the alleviation of the band tail states

for device-G.[2] The photoluminescence (PL) was further implemented to study the effect of the band tail states. As shown in Figure 4f, the difference of E_{PL} and E_g was 0.06, 0.05, 0.01 eV respectively in the case of H, G, D. The literature suggests in a clean semiconductor material with low defect concentration, the room-temperature E_{PL} is usually slightly higher than E_g, however, the band tail states will make a red shift of PL peak relative to E_g, that is, the decrease of band gap.[50] In these three devices, the minimal PL peak shift for device-D corresponded to the minimal E_u, which was in good agreement with the literature.[50] Subsequently, the minority carrier lifetime was measured via time-resolved photoluminescence (TRPL) with 532 nm laser to investigate the influence of the nonradiative recombination caused by defects. The lifetime τ_1 and τ_2 and specific fitting process were presented in **Table S7 and Supplementary Note 1** respectively. The average minority carrier lifetime for device-H, G, and D was 1.94, 3.78 and 2.37 ns respectively as shown in Figure 4g, which implies that the defect states at the interface and/or in the bulk were effectively inhibited for device-G.[4, 12, 51] Thus, the characterizations reflecting the information of the defect states such as the energy level and concentration were further performed. Above all, the heterojunction was probed by the Capacitance-Voltage (C–V) and Drive-Level Capacitance Profiling (DLCP) measurements. As far as we know, the difference between the values of C-V (N_{CV}) and DLCP (N_{DLCP}) at zero bias is the interfacial defect density (N_{IT}) at CAZTSSe/CdS interface.[52] The calculation processes of N_{CV} and N_{DLCP} was summarized in **Supplementary Note 2** and the corresponding results were displayed in Figure 4h and **Table 2**. Apparently, device-G owned the lowest interfacial defect density (5.60×10^{14} relative to 9.06×10^{14} of device-H and 1.35×10^{15} of device-D), which is beneficial to alleviating the interface recombination. In addition, the widest depletion region (the X value at zero bias) for device-G facilitated the separation of electron–hole pairs.

2.5. Defect Properties of device-H, G, and D

In order to verify the conjecture in the above sections, temperature-dependent admittance spectroscopy (AS) and capacitance-mode deep-level transient spectroscopy

(C-DLTS) were further carried out on these three devices to detect specific defects. The admittance spectra in the temperature range of 110–300 k and the C-DLTS spectra were shown in **Figure S9** and **Figure 5**c respectively. It has been reported that the positive and negative peaks in DLTS spectra separately represent majority carrier traps and minority carrier traps,[13, 53] and the corresponding Arrhenius plots reflecting the defect energy levels of AS and C-DLTS were presented in Figure 5a and d respectively. Figure 5b exhibits the defect density spectra of AS and the corresponding Gaussian fit curves obtaining the defect concentration. The specific calculation process was summarized in **Supplementary Note 3**. For the defect energy level and concentration of DLTS, they only need to be fitted by software attached to DLTS test system. The detailed information about the defects were shown in **Table 3**, where E_a is the trap activation energy and N_T is the trap concentration. To our knowledge, E_a values of Cu_{Zn} antisite acceptor defects are in the range of 0.10–0.20 eV [relative to the the valence band maximum (VBM)] and the E_a values of Cu_{Sn} antisite acceptor defects are in the range of 0.25–0.42 eV (relative to the VBM).[25] Besides, the defects with E_a in the range of 0.20–0.40 eV [relative to the the conduction band minimum (CBM)] can be assigned to [$2Cu_{Zn}$+Sn_{Zn}] defect clusters.[54] In fact, [$2Cu_{Zn}$+Sn_{Zn}] cluster is a donor−acceptor fully compensated defect, so it cannot produce any carriers, but it can produce high density unoccupied defect states below the conduction band edge.[55] Meanwhile, the formation energy of [$2Cu_{Zn}$+Sn_{Zn}] defect cluster is the lowest except Cu_{Zn} antisite defects.[56] Surprisingly, [$2Cu_{Zn}$+Sn_{Zn}] defect clusters were not detected in device-D, but it did not make $V_{oc,def}$ low enough. Rey et al. and Ma et al. confirmed that the band tail states are directly related to [$2Cu_{Zn}$+Sn_{Zn}] defect clusters, and Cu-Zn disorder is not directly responsible for the large tailing of the kesterite.[55, 57] This indicates that the reduction of the $V_{oc,def}$ was not directly related to the suppression of [$2Cu_{Zn}$+Sn_{Zn}] defect clusters here. But there is no doubt that the reduction of energy level and concentration of [$2Cu_{Zn}$+Sn_{Zn}] defect clusters is beneficial to alleviate the band tail states by combining the results of E_u. And [$2Cu_{Zn}$+Sn_{Zn}] defect clusters were gradually suppressed from device-H to device-G to device-D with the increase of Se content of

the selenization ingredients mainly because the formation energy of the isolated deep donor defects Sn_{Zn}^{2+} are higher under higher Se content, which makes the concentration of Sn_{Zn}^{2+} lower.[56] In addition, the concentration of the shallow Cu_{Zn} defects and Cu_{Sn} deep-level defects was very high in device-D, and especially the concentration of Cu_{zn} antisite defects was on the order of magnitude of 10^{16}. On the contrary, the concentration of Cu_{zn} and Cu_{Sn} defects in device-H was lower, but the defect levels of them were deeper than those in device-D. The high concentration and/or deep energy level of defects would both exacerbate carrier recombination in that defects more easily act as carrier recombination centers. However, in device-G, the concentration and energy level of the defects were effectively reduced as follows. Firstly, the energy levels of Cu_{Zn} and Cu_{Sn} defects were the lowest among the three, 124 and 261 meV respectively. Secondly, the concentration of Cu_{Zn} defects was 3.46×10^{15} cm^{-3}, which was well below 8.05×10^{15} and 1.03×10^{16} cm^{-3}. Thirdly, the concentration of Cu_{Sn} antisite defects (2.08×10^{12} cm^{-3}) was lower than that of device-D (4.11×10^{12} cm^{-3}), but the concentration of Cu_{Sn} defects was lowest in device-H. Even so, compared with device-H, there was great progress that the reduction of 77 meV in the energy level of Cu_{Sn} defects from 338 meV to 261 meV for device-G. The lowest density of Cu_{Sn} antisite defects in device-H can be ascribed to the high concentration of $[2Cu_{Zn}+Sn_{Zn}]$ defect cluster, yet the concentration of these two defects was balanced in device-G. The above results indicate that the recombination of photon-generated carriers was effectively suppressed under the selenizaition condition of G. According to the literature, the shallower energy level and lower concentration of Cu_{Zn} and Cu_{Sn} antisite defects are attributed to the weaker hybridization under the condition of G.[56] By the above analyses for the defects, we reasonably believe that another reason for the decrease of $V_{oc,def}$ was the reduction of cation disorder level except the appropriate band bending at the GBs and the reduced interface recombination in device-G.[4, 56] To show the energy levels and concentrations of these defects clearly, the schematic diagram was drawn and presented in Figure 5f~h. The position of the peak corresponds to the position of the defect energy level and the area of the peak corresponds to the

concentration of the defect. Duan et al. reported that there is stronger recombination due to the defects with higher density and deeper energy level in the sulfur-rich device.[24] The phenomenon that the energy level and concentration of defects rise simultaneously with the increase of S content seems to contradict our results, but it does not in fact because our devices were selenium-rich, whose band gaps were 1.14, 1.14, and 1.09 eV. Duan's subjects, however, were the solar cells with the band gaps of 1.15, 1.35 and 1.50 eV. Meanwhile, the schematic electronic structure of the band alignment at CAZTSSe/CdS heterojunction interface was displayed in Figure 5e based on the Ultraviolet Photoelectron Spectroscopy (UPS). The UPS plots were shown in **Figure S10** and the calculation process of work function was added in the **Supplementary Note 4**. Haight et al. reported that the high efficiency solar cells were often obtained in the case of the spike-like type with the positive conduction band offsets (CBO) of 0~0.4 eV at CZTSSe/CdS interface.[58] For device-H, G and D, their band alignments at CAZTSSe/CdS interface all presented spike-like type and the CBO were 0.18, 0.22, and 0.29 eV respectively which were in the suitable range of 0~0.4 eV. But compared with device-G, there was higher interfacial defect density in both device-H and D. Besides, too small CBO value of device-H could increase interface recombination and overlarge CBO value of device-D was not conducive to electron tunneling. Therefore, under the condition of G, the lowest interfacial defect density and appropriate CBO value enabled the interface recombination to be effectively inhibited, and thus the best performance.

2.6. Analysis of Suppressed Defects in device-G

Although the dEQE/dE versus E plot exhibits the same band gap for device-H(SnS+Se) and G(SnS+$SnSe_2$+Se), they show great differences in the defect states. To clarify the reasons for the significant reduction of defect energy level and concentration for the champion device when $SnSe_2$ was added to SnS in the selenization process, high-angle annular dark-field scanning transmission electron microscopy (HAADF-STEM) and energy-dispersive spectroscopy (EDS) elemental line scans were further performed on the champion device-G and the reference device-H. The cross-sectional TEM images

and the results of EDS elemental line scans were shown in **Figure 6**a and b. Obviously, in the cross-sectional TEM images, the tri-layer sandwich structure of device-H consists of middle fine-grained layer, and top and bottom large grain layers; the bi-layer structure of device-G consists of dense macrocrystalline layer and bottom thin fine-grained layer. They were both consistent with cross-sectional SEM images. In addition, the elemental distribution of device-G was more uniform than that of device-H, especially S and Se, which were presented separately in Figure 6c and the corresponding S/Se plots were shown in Figure 6d. The calculated formula of band gap of $Cu_2ZnSn(S_{1-x}Se_x)_4$ at different composition (x) using the Heyd-Scuseria-Ernzerhof (HSE) functional proposed by Chen et al. is as follows:

$$E_g(x) = (1-x)E_g(CZTS) + xE_g(CZTSe) - bx(1-x) \quad (26)$$

where E_g(CZTS) = 1.5 eV, E_g(CZTSe) = 0.96 eV, b = 0.07 eV.[59] It should be pointed out that there was little influence on the band gap when 5% Ag was incorporated into CZTSSe bulk as reported by Gong et al,[13] so the above calculation formula of band gap of CZTSSe was used directly here and thus the variation of band gap of CAZTSSe bulk was obtained by the value of S/Se, as shown in Figure 6d. Under the HSE functional model, the band gap of device-G was basically consistent with that by EQE, but the band gap of device-H was much different from that calculated by EQE. The band gap calculated by EQE reflects overall band gap of absorber, but the local band gap of CAZTSSe bulk was obtained by the values of S/Se from EDS elemental line scans. This indicates that the composition fluctuation of S and Se element inevitably brought local band gap fluctuation in device-H. We know that the band gap fluctuation is one of the main causes of the band tail states, and consequently device-H owned a larger E_u value than device-G as shown in Figure 4e, which also inevitably exacerbated carrier recombination in the unoccupied defect states below the conduction band edge.[55, 57] In addition, the heterogeneous distribution of elements especially S and Se in the absorber of device-H may be the main reason for its higher defect concentration and deeper defect level. And we individually took a set of atomic fraction data in the least fluctuating region of EDS plots for device-H and device-G as shown in **Table 4**.

The ratios of Ag/(Ag+Cu), Cu/(Zn+Sn) and Zn/Sn in these two devices were similar to the original stoichiometric ratio (Ag/(Ag+Cu) = 5%, Cu/(Zn+Sn) = 0.775, and Zn/Sn = 1.2), but the offsets of device-G was smaller. In particular, in device-G, the unaltered ratio of Zn/Sn relative to the original ratio and the decrease of Zn/Sn ratio compared with device-H indicate that Sn loss due to the decomposition of CZTSSe was effectively inhibited. To sum up, the selenization condition of G greatly improved the elemental distribution of absorber, making the composition more homogeneous, and thus a stable chemical environment was provided in the bulk for higher efficiency kesterite solar cells. Furthermore, high-resolution TEM (HRTEM) and selected-area electron diffraction (SAED) were performed to study the differences of the interplanar spacing in CAZTSSe lattice for these two devices. Figure 6e exhibits (112), (312) and (200) crystal plane with the interplanar spacing of 0.322 nm, 0.168 nm, 0.283 nm in device-H, and Figure 6f exhibits (112), (312) and (204) crystal plane with the interplanar spacing of 0.326 nm, 0.169 nm, 0.200 nm in device-G. We know that the interplanar spacing of CZTSe is wider than that of CZTS by their XRD standard card due to the larger atomic radius of Se (1.60 Å) relative to S (1.04 Å).[21, 60] Therefore, the increase of the interplanar spacing of (112) and (312) plane demonstrates that although device-G and H had the same band gap, S content of device-G was indeed less than that of device-H in the local area of bulk as shown in Figure 6c because of the heterogeneous distribution of S and Se in device-H. Besides, the enlarged crystal lattice diagrams were presented in **Figure S11**b and c corresponding to the insets of Figure 6e and f.

3. Conclusion

In this work, to avoid the introduction of excess S resulting in plenty of defects, the combination strategies of SnS and Sn or SnSe or $SnSe_2$ were first put forward. Intermediate phase $SnSe_{2(1-x)}S_{2x}$ and S_2 vapor turned out to be formed under the above three conditions through the analyses of XRD and Raman. According to the decomposition reactions of SnS, SnSe, SnS_2 and $SnSe_2$, the Sn-contained vapor inhibiting Sn loss was attributed to the gaseous $SnSe_3$ from the decomposition of SnSe and $SnSe_2$. Therefore, the joint effects of the products $SnSe_{2(1-x)}S_{2x}$ and S_2 vapor was

reflected in the following two aspects: 1) S from S_2 vapor incorporated into CZTSSe bulk to enlarge the band gap and thus lifted the V_{oc}; 2) gaseous $SnSe_3$ from the decomposition of $SnSe_2$ during selenization was indirectly involved in the selenization reactions to promote the prodution of CZTSSe and inhibit the decomposition of CZTSSe, and thus the increase of V_{oc}. However, due to the most suitable supply rate of S_2 vapor and gaseous $SnSe_3$ under the condition (SnS+$SnSe_2$+Se), grain fusion was effectively promoted and thus the macrocrystalline absorber with the largest and densest grains, and the thinnest $MoSe_2$. In addition, the real reasons for the decrease of $V_{oc,def}$ under the selenization condition (SnS+$SnSe_2$+Se) were the appropriate band bending at the GBs, suppressed interface recombination and reduction of cation disorder level, rather than the band tail states. The results of TEM-attached EDS elemental line scan indicate that when $SnSe_2$ was added to SnS, the reduction of defect energy level and concentration was because of more homogeneous elemental distribution of CAZTSSe bulk, especially S and Se, and thus a stable chemical environment, which also effectively alleviated band gap fluctuation. Finally, a champion solar cell with an efficiency of 12.89%, $V_{oc,def}$ of 350 mV and V_{OC}/V_{oc}^{SQ} of 60.91% under the selenization condition (SnS+$SnSe_2$+Se) was achieved, which were the optimum for ambient air-processed CZTSSe solar cells and at the forefront of high efficiency cells of other solvent systems. The V_{oc} (546 mV) with a band gap of 1.14 eV was an encouraging result for kesterite solar cells. The unveiled reaction mechanisms of optimized selenization atmosphere have guiding significance for further ameliorating selenization process and improving the efficiency of the kesterite solar cells. In the future, appropriate reduction of Sn component under the condition (SnS+$SnSe_2$+Se) is expected to suppress the Sn_{Zn}-based defect clusters such as [$2Cu_{Zn}$+Sn_{Zn}], optimize the band edge electronic structure, and thus achieve higher photoelectric conversion efficiency.

4. Experimental Section

Preparation of CAZTS Precursor Solution: According to the mole ratios of 0.775 and 1.2 for Cu/(Zn + Sn) and Zn/Sn respectively, Sn^{4+} CZTS precursor solution was

prepared by dissolving CuCl, $Zn(CH_3COO)_2 \cdot 2H_2O$, $SnCl_4 \cdot 5H_2O$, and $SC(NH_2)_2$ in 2-Methoxyethanol, and Sn^{2+} CZTS precursor solution was prepared by dissolving $Cu(CH_3COO)_2 \cdot H_2O$, $ZnCl_2$, $SnCl_2 \cdot 2H_2O$, and $SC(NH_2)_2$ in 2-Methoxyethanol. These ingredients were stirred about 2 hours in the water bath kettle set at 60 °C until the solutions became clear and dark yellow. Then Sn^{4+} and Sn^{2+} CZTS precursor solutions were diluted to half of its original concentration and were mixed evenly in a 1: 1 ratio. In addition, Ag^+ solution was prepared by dissolving AgCl and $SC(NH_2)_2$ in dimethyl formamide (DMF), which were also stirred about 2 hours in the water bath kettle set at 60 °C until the solution became clear. The mole ratio of AgCl to $SC(NH_2)_2$ was 1: 2. Subsequently, Ag^+ solution was dropped into the mixed precursor solution as final precursor solution and were stirred for mixing evenly. The different Ag ratios ($\frac{n(Ag)}{n(Ag)+n(Cu)}$ = 0%, 2%, 3%, 4%, 5%, 6%, 7%, 8%, 11%) were experimented. The preparation of CAZTS precursor solution was all operated in air.

Fabrication of CAZTSSe Thin Film: The CAZTS precursor solution was spin-coated on precleaned molybdenum (Mo)-coated soda–lime glass (Mo-SLG) substrates with 3000 rpm for 20 s. And the wet film was immediately annealed at 280 °C for 2 min on a hot plate. The coating–annealing-cooling cycle was repeated 10 times. The preparation of CAZTS precursor films was also operated in air. Subsequently, the selenization process was conducted. CAZTS precursor films and different selenization ingredients (Se, Sn+Se, SnSe+Se, $SnSe_2$+Se, SnS+Sn+Se, SnS+SnSe+Se, SnS+$SnSe_2$+Se, SnS+Se, SnS_2+Se) were placed into a graphite box with a lid. The inside size of the graphite box is 6.8×6.8×1.6 cm^3. For these nine selenization ingredients, four important points are listed here: 1) Sn, SnSe, $SnSe_2$, SnS and SnS_2 are all powder except Se granules, and the powders and Se granules were placed separately; 2) the total mass of Se granules under all conditions was the same (1.80 g, the mass of each Se granule is about 0.05 g), which were placed in nine quartz boats on average; 3) the total mole amount of Sn was the same under all conditions except only Se granules condition, and the standard of the total mole amount is Sn contained in 0.25g SnS. 4) the mole ratio of SnS:Sn,

SnS:SnSe and SnS:$SnSe_2$ is 1:2 under the conditions of SnS+Sn+Se, Sn+SnSe+Se and SnS+$SnSe_2$+Se, in order not to introduce too much S. The quartz tube was purged three times by argon prior to selenization after the graphite box was placed in the tube of the rapid thermal processing furnace. Then the furnace was heated from room temperature to 80 °C in 15 s and held 80 °C for 2 min. The second stage of heating is that the furnace was heated from 80 °C to 555 °C in 110 s and held 555 °C for 15 min. Later, the furnace naturally cooled down to room temperature. Argon gas flowed throughout the selenization process and the Ar flow rate is 80 sccm. The pressure in the graphite box was about 1 atm.

Device Fabrication: Cadmium sulfide (CdS) buffer layer about 60 nm was deposited on CAZTSSe thin films by using chemical bath deposition (CBD). The CBD process lasted 9 min at 80 °C in the solution contained $CdSO_4$ (0.015 M, 20 mL), thiourea (0.75 M, 20 mL), ammonia (14.8 M, 20 mL), and deionized water (140 mL). Subsequently, the Indium Tin Oxide (ITO) window layer was directly sputtered on CdS by radio frequency (RF) magnetron sputtering for 25 min under suitable O_2/Ar ratio atmosphere (O_2/Ar ≈ 2%). The working power was 120 W, and the working pressure was 0.4 Pa. Then the top contact Ag gate electrodes were deposited with the help of a shadow mask by thermal evaporation. Finally, the device was divided by mechanical scribing and CAZTSSe thin film solar cells with active area of 0.135 cm^2 (glass/Mo/CAZTSSe/CdS/ITO/Ag) were fabricated.

Characterization: X-ray diffraction (XRD) patterns of the powders and films were performed on an X-ray powder diffractometer (Model: Empyrean; Manufacturer: PANalytical) with Cu K_α as the radiation source from 10° to 80°. Raman spectra of the powders and films were collected by Raman spectrometer (Renishaw inVia) with an excitation wavelength of 532 nm. The morphology and cross-section images of the absorbers were obtained by scanning electron microscope (SEM) (SUPRA 55), and the chemical composition of the samples was analyzed by energy dispersive spectroscopy (EDS) (BRUKER QUANTAX 200). The contact potential difference of the films was conducted by Kelvin probe force microscopy (KPFM) measurements (Model:

Dimension Icon; Manufacturer: Bruker) with the SCM-PIT probe under the peakforce KPFM-AM scan mode. The scan rate was 1 Hz and the drive amplitude was 2000 mV. The dark and illuminated J–V characteristics of the devices were measured by a Keithley 2400 meter and a Zolix SS150 solar simulator calibrated with a certified Si cell under standard test condition (100 mW/cm^2, 25 °C, AM1.5G). External quantum efficiency (EQE) was examined by a Zolix solar cell QE/IPCE measurement system (Solar Cell Scan 100) with calibrated Si and InGaAs photodiodes as references. The photoluminescence (PL) and time-resolved photoluminescence (TRPL) were measured via a FluoTime 300 spectrograph with an excitation wavelength of 532 nm. The power of the laser is 50 mW. Capacitance–voltage (*C*–*V*) profiling and drive level capacitance profiling (DLCP) were carried out by a Keithley 4200A-SCS system with JANIS cryogenic platform. The *C*–*V* was conducted with the DC bias voltage from −0.5 V to 0.1 V under a dark condition at room temperature; the AC amplitude was 30 mV and the frequency was 500 kHz. The DLCP was conducted with the DC bias voltage from −0.25 V to 0 V and the AC amplitude from 20 mV to 140 mV at the frequency of 500 kHz. Admittance Spectroscopy measurement was carried out by Victor Digital LCR meter with the temperature range of 110 K to 300 K (10 K step) and the frequency range of 10^2 to 10^6 Hz. Deep-level transient spectroscopy (DLTS) was carried out by the FT-1030 HERA DLTS system configured with a JANIS VPF-800 cryostat controller. The scan temperature was from 105 K to 375 K. The reverse bias (V_R) of 0.35 V, pulse voltage (V_p) of -0.3 V, and pulse width of 1 ms were set. Ultraviolet Photoelectron Spectroscopy (UPS) was performed by PHI 5000 VersaProbe III with He I source (21.22 eV) under an applied negative bias of 9.0 V. The TEM lamella samples were prepared by the focused ion beam (FIB) with a microsampling system (FEI Xt Nova NanoLab 200). The cross-section TEM images and the elemental distribution of the devices were characterized by double Cs-corrected transmission electron microscope (model: Titan^3 Cubed Themis G2 300) equipped with EDS system. Electrochemical impedance spectroscopy (EIS) was measured by CHI660E electrochemical workstation.

Supporting Information

Supporting Information is available from the Wiley Online Library or from the author.

Acknowledgements

This work was supported by National Natural Science Foundation of China (62074102 and 62204067) China, Science and Technology plan project of Shenzhen (20220808165025003) China. Guangdong Basic and Applied Basic Research Foundation (2022A1515010979) China. The authors wish to acknowledge the assistance on (TEM/STEM/FIB) received from the Electron Microscope Center of the Shenzhen University.

Conflict of Interest

The authors declare no conflict of interest.

References

[1] W. Wang, M. T. Winkler, O. Gunawan, T. Gokmen, T. K. Todorov, Y. Zhu, D. B. Mitzi, *Adv. Energy Mater.* **2014**, 4, 1301465.

[2] Y. Gong, Y. Zhang, Q. Zhu, Y. Zhou, R. Qiu, C. Niu, W. Yan, W. Huang, H. Xin, *Energy Environ. Sci.* **2021**, 14, 2369.

[3] A. D. Collord, H. W. Hillhouse, *Chem. Mater.* **2016**, 28, 2067.

[4] Z. Su, G. Liang, P. Fan, J. Luo, Z. Zheng, Z. Xie, W. Wang, S. Chen, J. Hu, Y. Wei, C. Yan, J. Huang, X. Hao, F. Liu, *Adv. Mater.* **2020**, 32, 2000121.

[5] J. Fu, J. Fu, Q. Tian, H. Wang, F. Zhao, J. Kong, X. Zhao, S. Wu, *ACS Appl. Energy Mater.* **2018**, 1, 594.

[6] Y. Gong, Q. Zhu, B. Li, S. Wang, B. Duan, L. Lou, C. Xiang, E. Jedlicka, R. Giridharagopal, Y. Zhou, Q. Dai, W. Yan, S. Chen, Q. Meng, H. Xin, *Nat. Energy* **2022**, 7, 966.

[7] M. Nakamura, K. Yamaguchi, Y. Kimoto, Y. Yasaki, T. Kato, H. Sugimoto, *IEEE*

J. Photovoltaics **2019**, 9, 1863.

[8] W. Liu, H. Li, B. Qiao, S. Zhao, Z. Xu, D. Song, *Sol. Energy* **2022**, 233, 337.

[9] Z.-K. Yuan, S. Chen, H. Xiang, X.-G. Gong, A. Walsh, J.-S. Park, I. Repins, S.-H. Wei, *Adv. Funct. Mater.* **2015**, 25, 6733.

[10] Y. Qi, Q. Tian, Y. Meng, D. Kou, Z. Zhou, W. Zhou, S. Wu, *ACS Appl. Mater. Interfaces* **2017**, 9, 21243.

[11] Y.-F. Qi, D.-X. Kou, W.-H. Zhou, Z.-J. Zhou, Q.-W. Tian, Y.-N. Meng, X.-S. Liu, Z.-L. Du, S.-X. Wu, *Energy Environ. Sci.* **2017**, 10, 2401.

[12] Y. Sun, P. Qiu, W. Yu, J. Li, H. Guo, L. Wu, H. Luo, R. Meng, Y. Zhang, S. F. Liu, *Adv. Mater.* **2021**, 33, 2104330.

[13] Y. Gong, R. Qiu, C. Niu, J. Fu, E. Jedlicka, R. Giridharagopal, Q. Zhu, Y. Zhou, W. Yan, S. Yu, J. Jiang, S. Wu, D. S. Ginger, W. Huang, H. Xin, *Adv. Funct. Mater.* **2021**, 31, 2101927.

[14] H. Cai, L. Yao, Y. Xia, C. Dao, J. Li, L. Lin, Z. Huang, G. Chen, *Sol. Energy* **2019**, 193, 986.

[15] Y.-P. Lin, T.-E. Hsieh, Y.-C. Chen, K.-P. Huang, *Sol. Energy Mater. Sol. Cells* **2017**, 162, 55.

[16] P. K. Kannan, S. Chaudhari, S. R. Dey, *Mater. Today:. Proc.* **2020**, 21, 1787.

[17] T. Enkhbat, S. Kim, J. Kim, *ACS Appl. Mater. Interfaces* **2019**, 11, 36735.

[18] K.-J. Yang, D.-H. Son, S.-J. Sung, J.-H. Sim, Y.-I. Kim, S.-N. Park, D.-H. Jeon, J. Kim, D.-K. Hwang, C.-W. Jeon, D. Nam, H. Cheong, J.-K. Kang, D.-H. Kim, *J. Mater. Chem. A* **2016**, 4, 10151.

[19] D.-H. Son, S.-H. Kim, S.-Y. Kim, Y.-I. Kim, J.-H. Sim, S.-N. Park, D.-H. Jeon, D.-K. Hwang, S.-J. Sung, J.-K. Kang, K.-J. Yang, D.-H. Kim, *J. Mater. Chem. A* **2019**, 7, 25279.

[20] C.-H. Cai, S.-Y. Wei, W.-C. Huang, J. Lin, T.-H. Yeh, C.-H. Lai, *Sol. Energy Mater. Sol. Cells* **2016**, 145, 296.

[21] B. Xu, C. Ma, X. Lu, Y. Liu, Q. Zhang, Y. Chen, P. Yang, J. Chu, L. Sun, *Sol. Energy Mater. Sol. Cells* **2020**, 210, 110522.

[22] X. Lu, B. Xu, C. Ma, Y. Chen, P. Yang, J. Chu, L. Sun, *Sol. Energy* **2020**, 196, 597.

[23] F. Liu, C. Yan, J. Huang, K. Sun, F. Zhou, J. A. Stride, M. A. Green, X. Hao, *Adv. Energy Mater.* **2016**, 6, 1600706.

[24] H.-S. Duan, W. Yang, B. Bob, C.-J. Hsu, B. Lei, Y. Yang, *Adv. Funct. Mater.* **2013**, 23, 1466.

[25] G.-X. Liang, Z.-X. Yu, Z.-G. Xie, Y. He, J.-H. Lin, S. Chen, Z.-H. Zheng, J.-T. Luo, P. Fan, Z.-H. Su, H.-L. Ma, X.-H. Zhang, *Sol. RRL* **2021**, 5, 2100574.

[26] K. Liu, H. Liu, J. Wang, L. Feng, *Mater. Lett.* **2009**, 63, 512.

[27] A. Redinger, D. M. Berg, P. J. Dale, S. Siebentritt, *J. Am. Chem. Soc.* **2011**, 133, 3320.

[28] J. J. Scragg, T. Kubart, J. T. Wätjen, T. Ericson, M. K. Linnarsson, C. Platzer-Björkman, *Chem. Mater.* **2013**, 25, 3162.

[29] L. Yao, J. Ao, M.-J. Jeng, J. Bi, S. Gao, G. Sun, Q. He, Z. Zhou, Y. Zhang, Y. Sun, L.-B. Chang, *Crystals* **2018**, 9, 10.

[30] A. Weber, R. Mainz, H. W. Schock, *J. Appl. Phys.* **2010**, 107, 013516.

[31] T. Shimada, F. S. Ohuchi, B. A. Parkinson, *J. Vac. Sci. Technol. A* **1992**, 10, 539.

[32] Y. Wang, L. H. Le Huang, B. Li, J. Shang, C. Xia, C. Fan, H.-X. Deng, Z. Wei, J. Li, *J. Mater. Chem. C* **2017**, 5, 84.

[33] D. Walsh, S. Jandl, J. Y. Harbec, *J. Phys. C: Solid State Phys.* **1980**, 13, L125.

[34] C. Julien, H. S. Mavi, K. P. Jain, M. Balkanski, *Materials Science and Engineering* **1994**, B23, 98.

[35] A. J. Smith, P. E. Meek, W. Y. Liang, *J. Phys. C: Solid State Phys.* **1977**, 10, 1321.

[36] Y. Yan, T. Guo, X. Song, Z. Yu, Y. Jiang, C. Xia, *Sol. Energy* **2017**, 155, 601.

[37] D. G. Mead, J. C. Irwin, *Solid State Commun.* **1976**, 20, 885.

[38] H. Liu, K. K. Antwi, S. Chua, D. Chi, *Nanoscale* **2014**, 6, 624.

[39] X. Duan, C. Wang, Z. Fan, G. Hao, L. Kou, U. Halim, H. Li, X. Wu, Y. Wang, J. Jiang, A. Pan, Y. Huang, R. Yu, X. Duan, *Nano Lett.* **2015**, 16, 264.

[40] J. J. Scragg, P. J. Dale, D. Colombara, L. M. Peter, *ChemPhysChem* **2012**, 13, 3035.

[41] Q. Yu, J. Shi, L. Guo, B. Duan, Y. Luo, H. Wu, D. Li, Q. Meng, *Nano Energy* **2020**, 76.

[42] W. Wang, Z. Cao, H. Wang, J. Luo, Y. Zhang, *J. Mater. Chem. A* **2021**, 9, 26963.

[43] X. Zhao, D. Kou, W. Zhou, Z. Zhou, Y. Meng, Q. Meng, Z. Zheng, S. Wu, *J. Mater. Chem. A* **2019**, 7, 3135.

[44] Y. Zhao, X. Zhao, D. Kou, W. Zhou, Z. Zhou, S. Yuan, Y. Qi, Z. Zheng, S. Wu, *ACS Appl. Mater. Interfaces* **2021**, 13, 795.

[45] S. Wang, Z. Shen, Y. Sun, H. Li, K. Zhang, L. Wu, J. Ao, Y. Zhang, *ACS Appl. Mater. Interfaces* **2021**, 13, 12211.

[46] J. R. Sites, *Sol. Energy Mater. Sol. Cells* **2003**, 75, 243.

[47] J. R. SITES, P. H. MAUK, *Solar Cells* **1989**, 27, 411.

[48] S. S. Hegedus, W. N. Shafarman, *Prog. Photovoltaics Res. Appl.* **2004**, 12, 155.

[49] G. Liang, M. Chen, M. Ishaq, X. Li, R. Tang, Z. Zheng, Z. Su, P. Fan, X. Zhang, S. Chen, *Adv. Sci.* **2022**, 9, 2105142.

[50] T. Gokmen, O. Gunawan, T. K. Todorov, D. B. Mitzi, *Appl. Phys. Lett.* **2013**, 103, 103506.

[51] P. Fan, Y. He, G. Liang, Z. Xie, Z. Yu, J. Lin, S. Chen, Z. Zheng, J. Luo, Z. Su, *J. Mater. Chem. A* **2021**, 9, 25196.

[52] R. Tang, Z.-H. Zheng, Z.-H. Su, X.-J. Li, Y.-D. Wei, X.-H. Zhang, Y.-Q. Fu, J.-T. Luo, P. Fan, G.-X. Liang, *Nano Energy* **2019**, 64, 103929.

[53] R. Tang, S. Chen, Z. H. Zheng, Z. H. Su, J. T. Luo, P. Fan, X. H. Zhang, J. Tang, G. X. Liang, *Adv. Mater.* **2022**, 34, 2109078.

[54] Y. Qi, X. Zhao, Y. Liu, D. Kou, W. Zhou, Z. Zhou, S. Yuan, Y. Meng, S. Wu, *J. Mater. Chem. A* **2021**, 9, 2292.

[55] S. Ma, H. Li, J. Hong, H. Wang, X. Lu, Y. Chen, L. Sun, F. Yue, J. W. Tomm, J. Chu, S. Chen, *J. Phys. Chem. Lett.* **2019**, 10, 7929.

[56] S. Chen, A. Walsh, X. G. Gong, S. H. Wei, *Adv. Mater.* **2013**, 25, 1522.

[57] G. Rey, G. Larramona, S. Bourdais, C. Choné, B. Delatouche, A. Jacob, G. Dennler, S. Siebentritt, *Sol. Energy Mater. Sol. Cells* **2018**, 179, 142.

[58] R. Haight, A. Barkhouse, O. Gunawan, B. Shin, M. Copel, M. Hopstaken, D. B. Mitzi, *Appl. Phys. Lett.* **2011**, 98, 253502.

[59] S. Chen, A. Walsh, J.-H. Yang, X. G. Gong, L. Sun, P.-X. Yang, J.-H. Chu, S.-H. Wei, *Phys. Rev. B* **2011**, 83, 125201.

[60] S. C. Riha, B. A. Parkinson, A. L. Prieto, *J. Am. Chem. Soc.* **2011**, 133, 15272.

Table 1. Summary of device parameters of device-H, G and D

Device	PCE [%]	V_{oc} [V]	FF [%]	J_{sc} [mA cm^{-2}]	R_S [Ω cm^2]	R_{sh} [Ω cm^2]	J_0 [mA cm^{-2}]	n	E_u [meV]	E_g [eV]	V_{oc-def} [V]	V_{OC}/V_{oc}^{SQ}
device-H	11.60	0.508	64.99	35.14	1.03	1270	2.9E-4	1.75	26.08	1.14	0.388	56.68%
device-G	12.89	0.546	65.85	35.86	0.83	1270	6.7E-5	1.73	25.10	1.14	0.350	60.91%
device-D	11.35	0.477	62.41	38.14	1.38	1420	4.7E-4	1.84	21.37	1.09	0.373	56.14%

Table 2. Summary of the results derived from *C-V* and DLCP measurements

Device	N_{cv} [cm^{-3}]	N_{dl} [cm^{-3}]	Depletion width [nm]	Interface state response (relative values)
device-H	1.11×10^{16}	1.02×10^{16}	172	9.06×10^{14}
device-G	6.70×10^{15}	6.14×10^{15}	187	5.60×10^{14}
device-D	1.60×10^{16}	1.46×10^{16}	137	1.35×10^{15}

Table 3. Summary of defect properties measured by AS and C-DLTS

Device	Label	Possible defect	Activation energy E_a [eV]	Trap conc. N_T [cm^{-3}]
device-H	H1	Cu_{Zn}	E_V+0.176	8.05×10^{15}
	H2	Cu_{Sn}	E_V+0.338	7.40×10^{11}
	E1	$2Cu_{Zn}$+Sn_{Zn}	E_C-0.303	5.66×10^{12}
device-G	H1	Cu_{Zn}	E_V+0.124	3.46×10^{15}
	H2	Cu_{Sn}	E_V+0.261	2.08×10^{12}
	E1	$2Cu_{Zn}$+Sn_{Zn}	E_C-0.214	2.19×10^{12}
device-D	H1	Cu_{Zn}	E_V+0.166	1.03×10^{16}
	H2	Cu_{Sn}	E_V+0.336	4.11×10^{12}

Table 4. Element composition ratio of CAZTSSe absorbers detected by TEM-EDS elemental line scans

Device	Cu [at.%]	Ag [at.%]	Zn [at.%]	Sn [at.%]	S [at.%]	Se [at.%]	Ag/(Ag+Cu)	Cu/(Zn+Sn)	Zn/Sn	S/Se
Device-H	22.32	1.41	15.69	12.89	17.99	29.70	0.059	0.781	1.217	0.606
Device-G	22.87	1.35	16.05	13.36	16.38	29.99	0.056	0.778	1.201	0.546

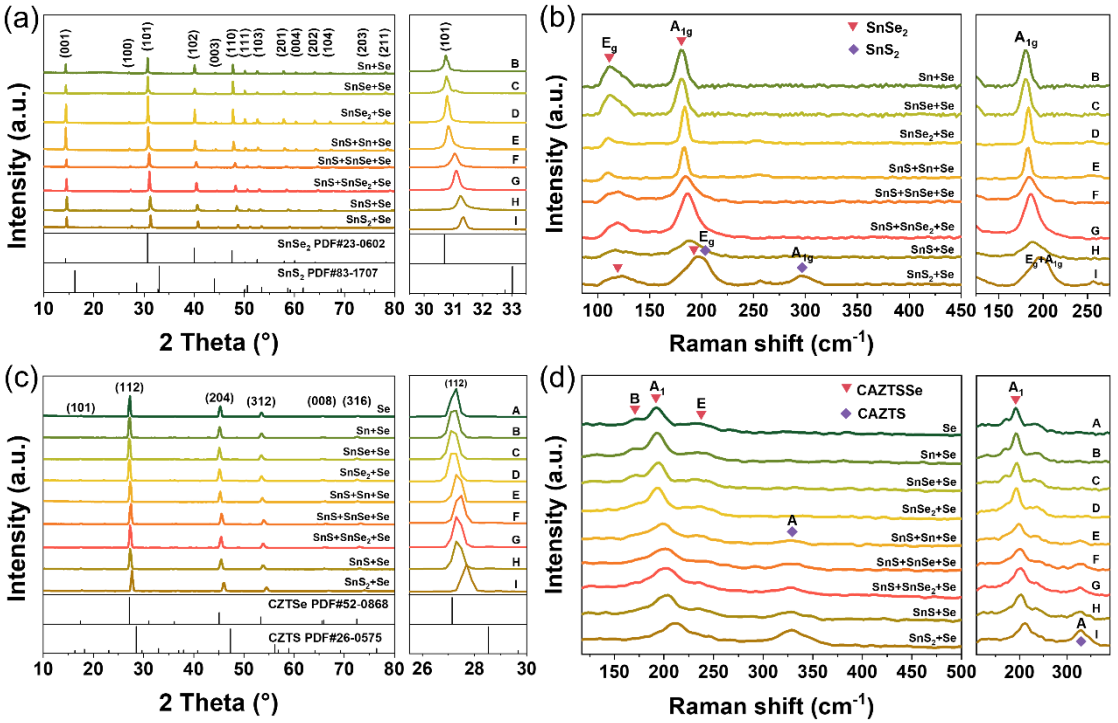

Figure 1. XRD patterns of (a) residual powders in the graphite box and (c) CAZTSSe thin films, Raman spectra of (b) residual powders and (d) CAZTSSe thin films under different selenization conditions.

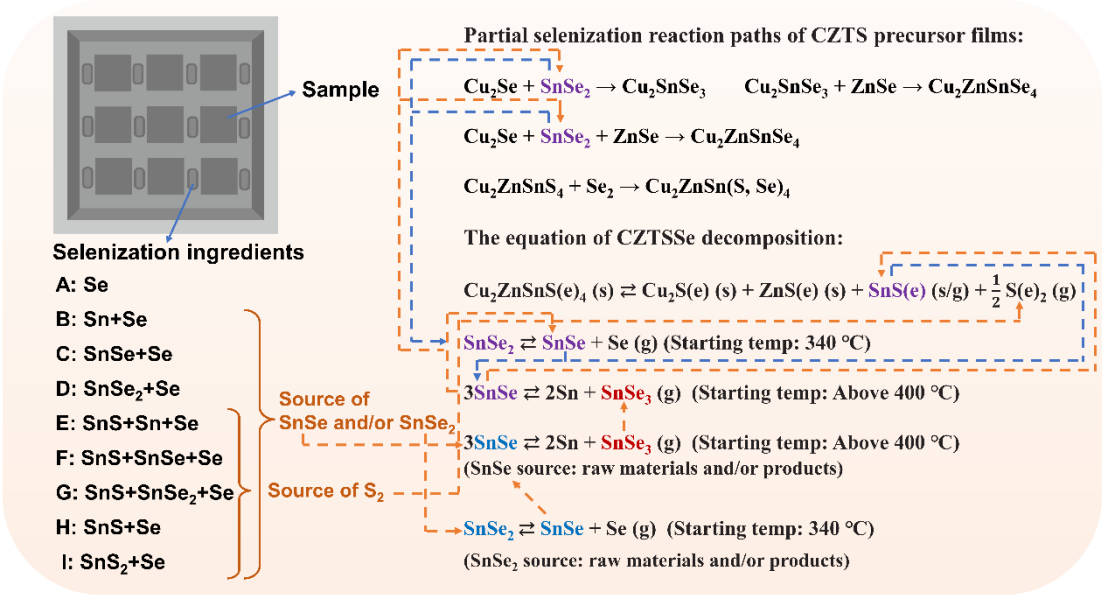

Scheme 1. Schematic diagram of the reaction mechanism of inhibiting Sn loss and replenishing S in the selenization process.

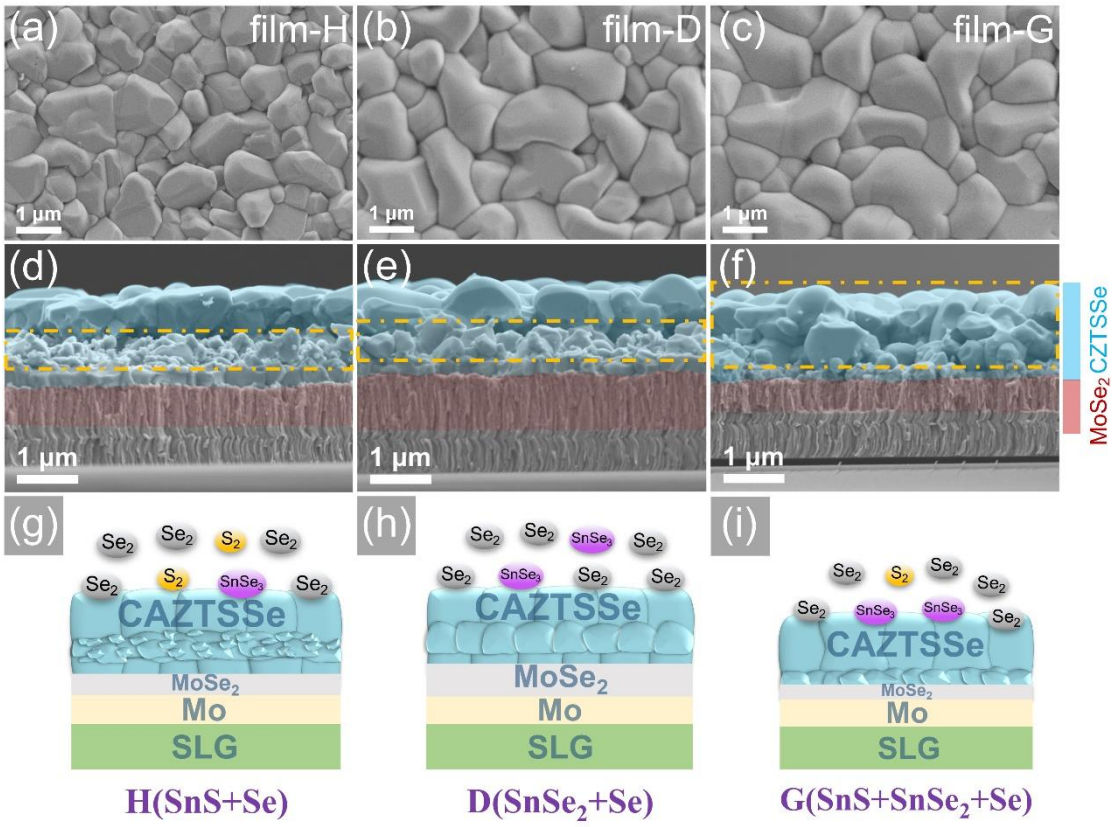

Figure 2. (a-c) The surface SEM images, (d-f) the cross-sectional images, and (g-i) schematic illustration of CAZTSSe thin films under the selenization conditions of

H(SnS+Se), D($SnSe_2$+Se), and G(SnS+$SnSe_2$+Se). (a)(d)(g), (b)(e)(h), and (c)(f)(i) correspond to film-H, film-D, and film-G, respectively.

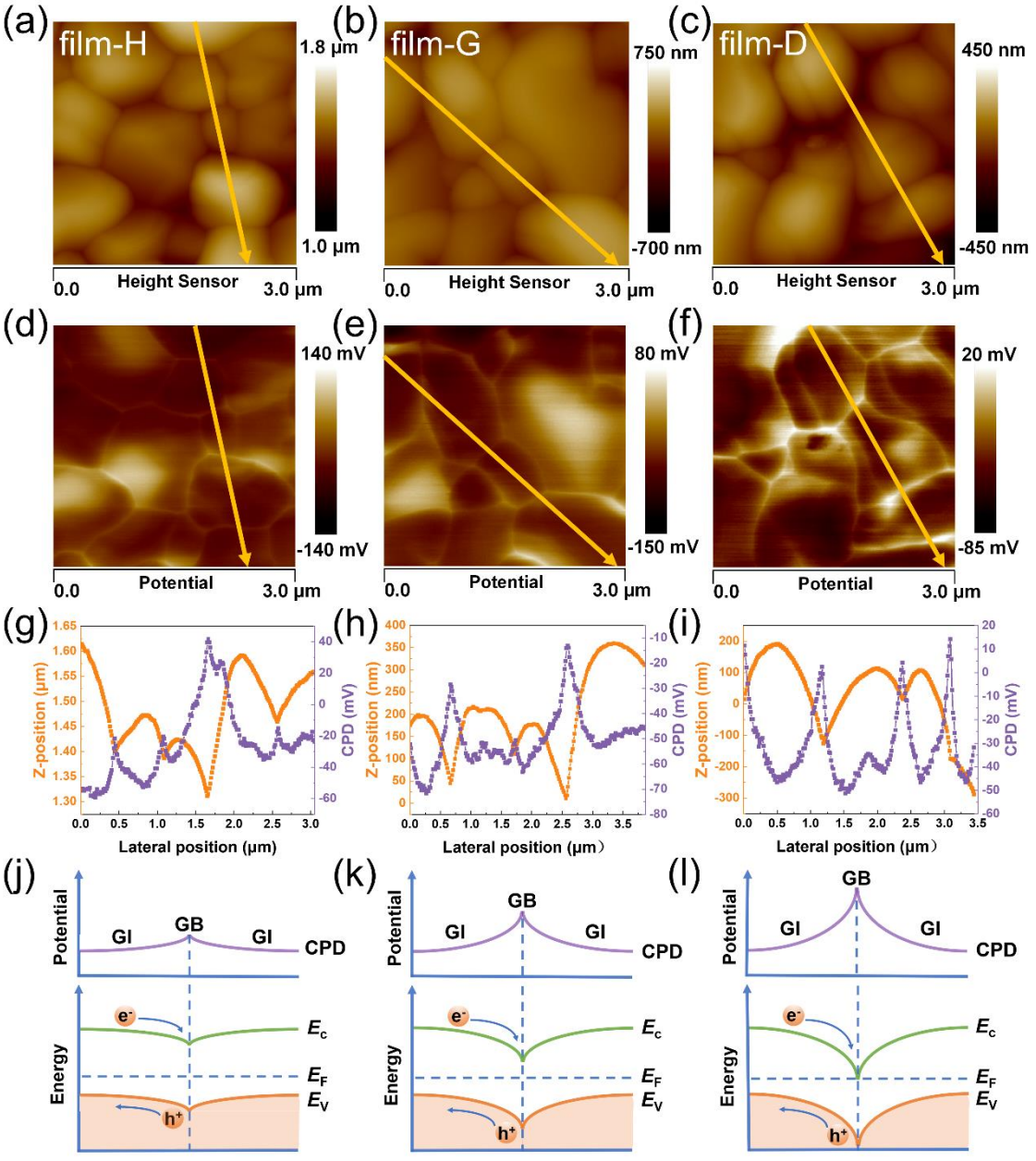

Figure 3. (a-c) AFM scanning surface topography, (d-f) CPD maps, (g-i) topography and potential line scans, (j-l) schematic diagrams of the energy band structure and CPD near the GBs for CAZTSSe thin films under the selenization conditions of H(SnS+Se), G(SnS+$SnSe_2$+Se), and D($SnSe_2$+Se). "e^-" represents electron; "h^+" represents hole. (a)(d)(g)(j), (b)(e)(h)(k), and (c)(f)(i)(l) correspond to film-H, film-G and film-D, respectively.

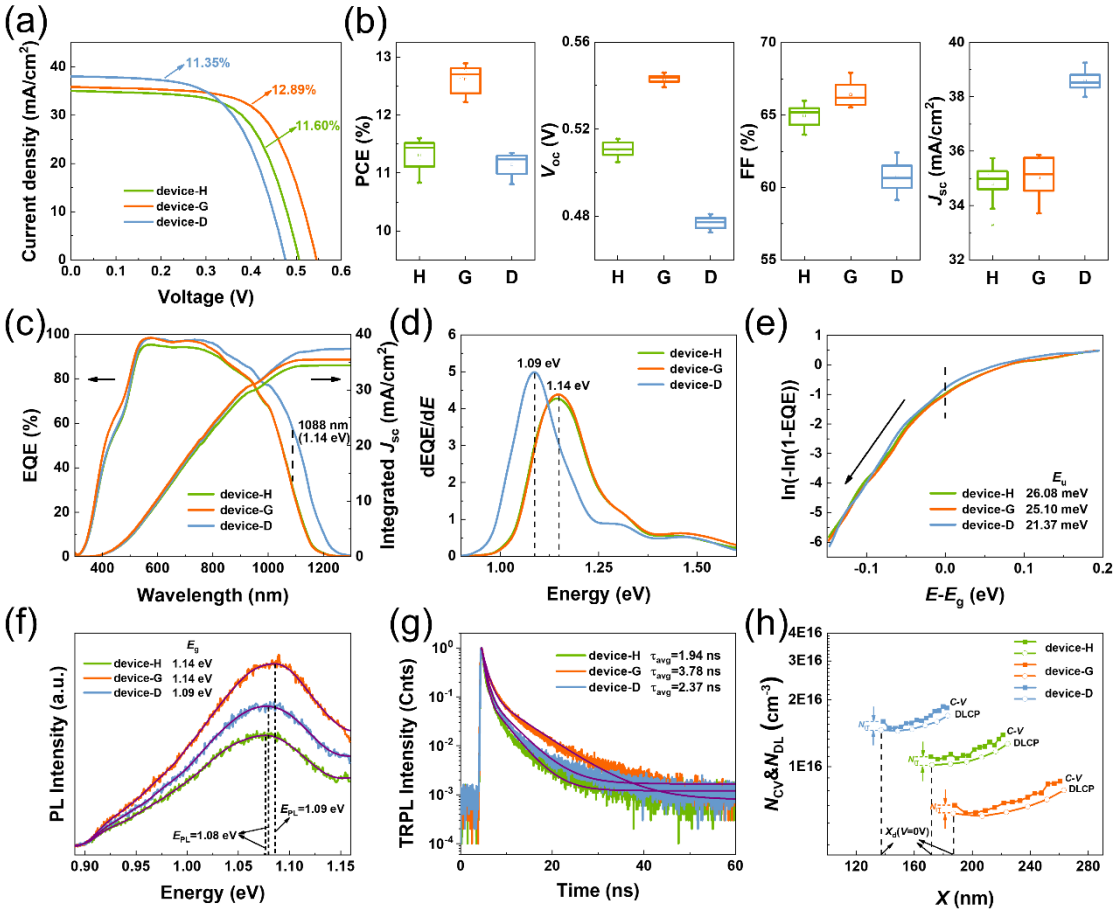

Figure 4. (a) *J–V* curves of the champion CAZTSSe solar cells and (b) the statistical distribution of the devices' photovoltaic parameters including PCE, V_{OC}, FF, and J_{SC} under the selenization conditions of H(SnS+Se), G(SnS+$SnSe_2$+Se) and D($SnSe_2$+Se); (c) EQE spectra of device-H, G and D; (d) The extraction of band gaps from dEQE/d*E* vs. *E* plots; (e) The extraction of the Urbach energy from ln(-ln(1-EQE)) vs. E-E_g plots; (f) PL spectra, (g) normalized TRPL spectra, (h) *C-V* and DLCP profiles of device-H, G and D.

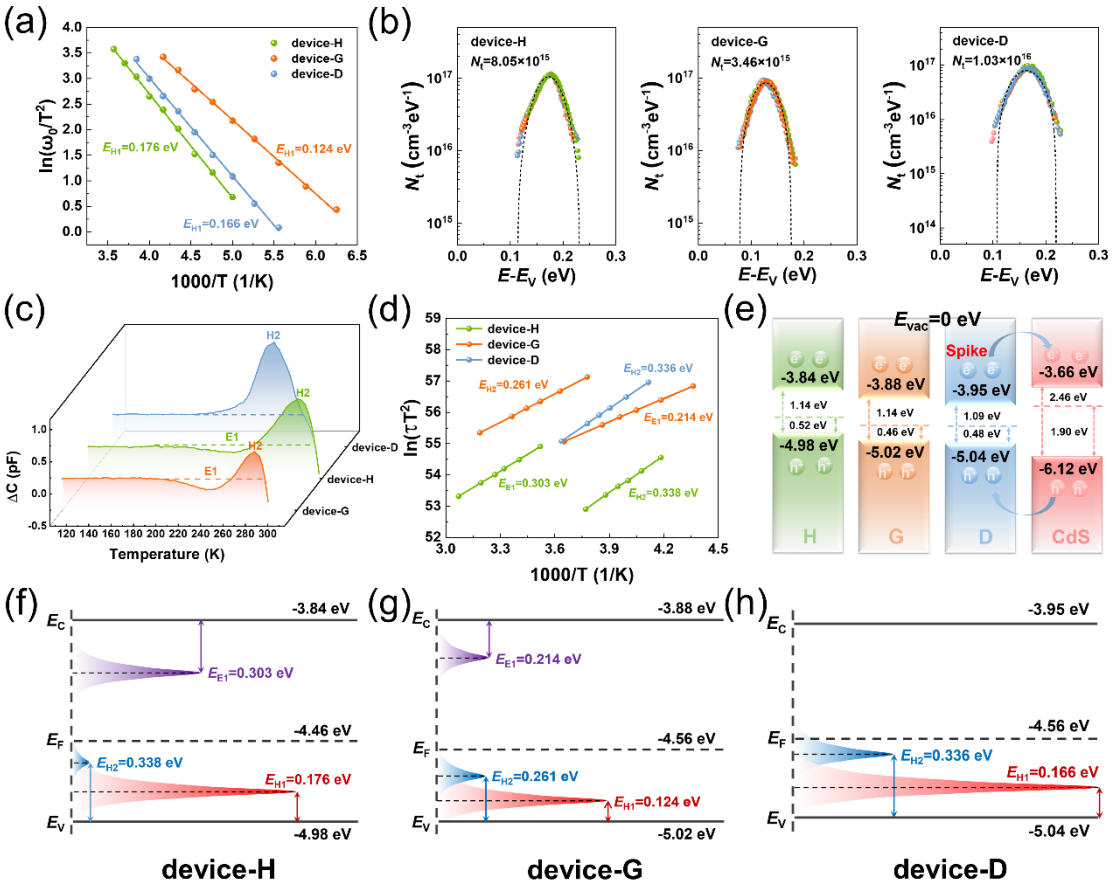

Figure 5. (a) The Arrhenius plots and (b) the defect density spectra derived from admittance spectra; (c) C-DLTS spectra; (d) The Arrhenius plots derived from C-DLTS spectra and corresponding to the peaks of DLTS spectra; (e) Schematic band alignment including the valence band, Fermi level, and conduction band of CAZTSSe/CdS derived from UPS. "e^-" represents electron; "h^+" represents hole. The schematic diagram of the band energy levels and defect energy levels of (f) device-H(SnS+Se), (g) device-G(SnS+$SnSe_2$+Se), and (h) device-D($SnSe_2$+Se).

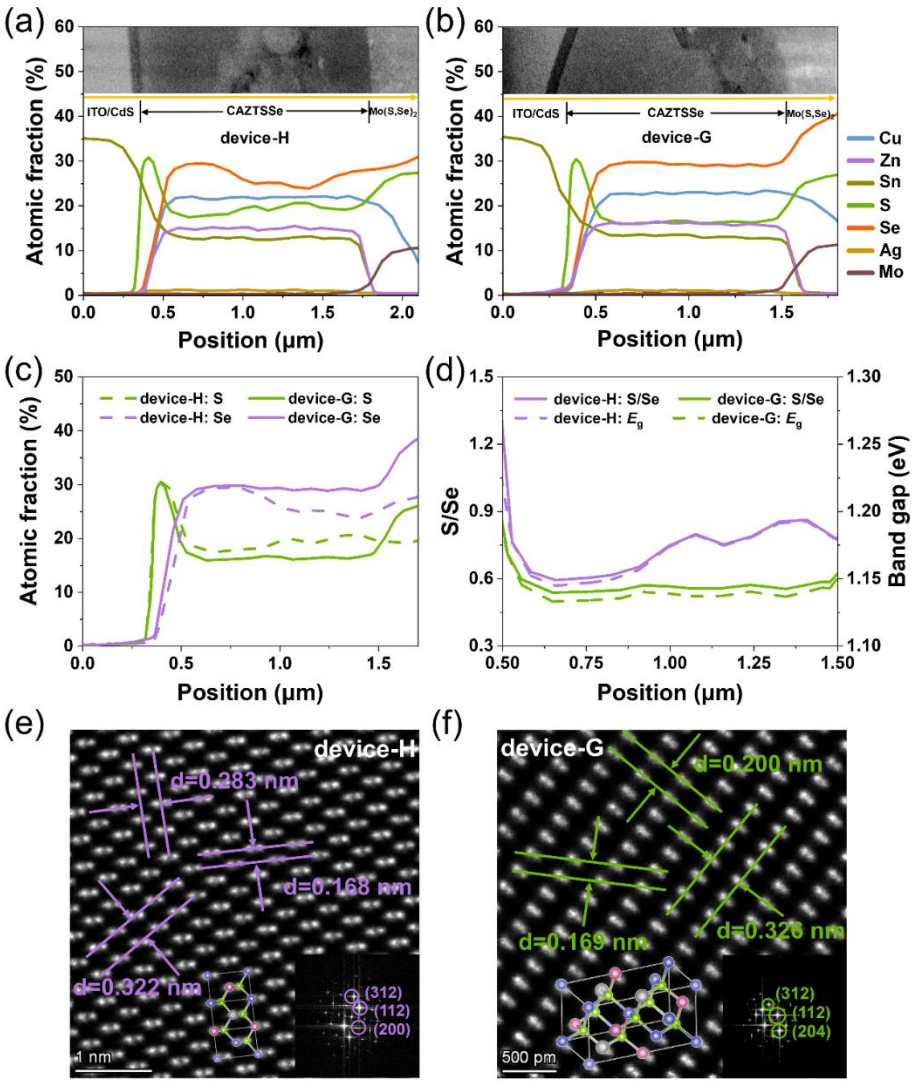

Figure 6. TEM-EDS elemental line scan profiles across (a) device-H and (b) device-G. The corresponding cross-sectional TEM images were shown in the insets of (a) and (b). (c) TEM-EDS line scan results of S and Se, (d) the values of S/Se and (d) corresponding band gaps derived from S/Se for device-H and device-G; High-resolution TEM images of (e) device-H and (f) device-G. The crystal lattice diagrams and selected-area electron diffraction patterns were inset (e) and (f).

Table of Contents:

The combination strategies of SnS and Sn or SnSe or $SnSe_2$ during selenization annealing process are first put forward. And the pathway of inhibiting Sn loss by gaseous $SnSe_3$ is first clarified. When $SnSe_2$ is added to SnS, grain fusion is effectively promoted and carrier recombination is effectively suppressed, and thus state-of-the-art ambient air-processed kesterite device with 12.89% efficiency.

ToC Figure

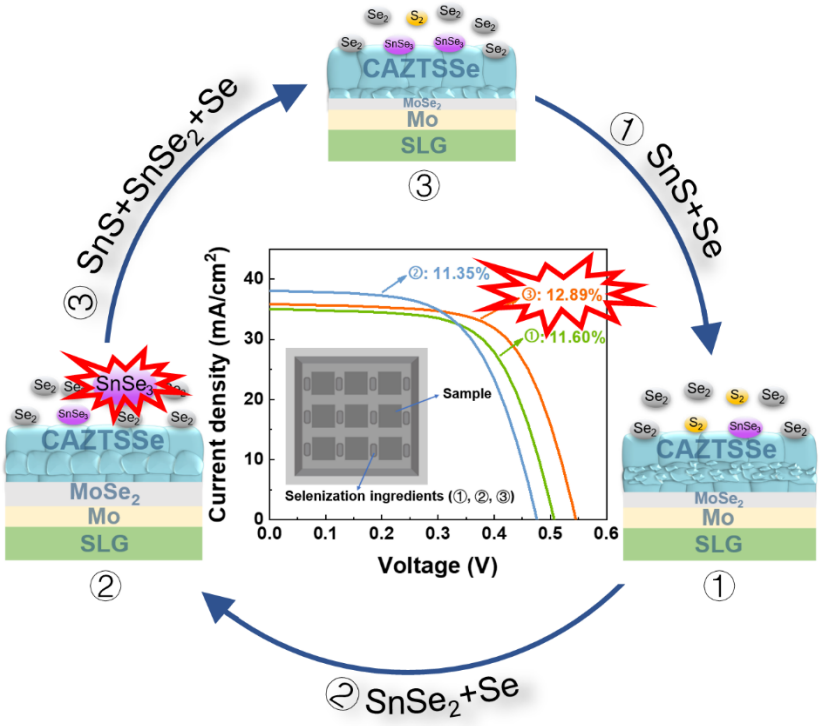

Supporting Information

Unveiling the Selenization Reaction Mechanisms in Ambient Air-processed Highly Efficient Kesterite Solar Cells

Zixuan Yu,Chuanhao Li, Shuo Chen, Zhuanghao Zheng, Ping Fan, Yingfen Li, Manlin Tan, Chang Yan, Xianghua Zhang,Zhenghua Su, and Guangxing Liang**

Table S1. Summary of photovoltaic parameters of the champion solar cells without and with 5% Ag under the selenization conditions of A and H

Device	V_{oc} [V]	FF [%]	J_{sc} [mA cm^{-2}]	PCE [%]
No Ag, A	0.460	58.74	39.11	10.57
5% Ag, A	0.474	60.65	39.12	11.25
No Ag, H	0.505	63.64	34.28	11.02
5% Ag, H	0.508	64.99	35.14	11.60

Table S2. The positions of (101) Peak of XRD patterns of residual powders in the graphite box under the selenization conditions of B(Sn+Se), C(SnSe+Se), D($SnSe_2$+Se), E(SnS+Sn+Se), F(SnS+SnSe+Se), G(SnS+$SnSe_2$+Se), H(SnS+Se), I(SnS_2+Se)

Sample	2 Theta of (101) Peak (°)
B	30.74
C	30.78
D	30.80
E	30.84
F	31.06
G	31.10
H	31.25
I	31.34

Table S3. The positions of Raman peaks of E_g and A_{1g} modes of $SnSe_2$ and SnS_2 for the residual powders under the selenization conditions of B, C, D, E, F, G, H, I

Sample	$SnSe_2$ Raman Shift (cm^{-1})		SnS_2 Raman Shift (cm^{-1})	
	E_g	A_{1g}	E_g	A_{1g}
B	111.78	180.87	\	\
C	111.86	181.24	\	\
D	110.20	183.67	\	\
E	110.20	183.51	\	\
F	117.61	185.10	\	\
G	118.97	186.69	\	\
H	117.69	189.25	\	\
I	123.13	198.63		298.22

Table S4. The positions of (112) Peak of XRD patterns of CAZTSSe thin films under the selenization conditions of A(Se), B(Sn+Se), C(SnSe+Se), D($SnSe_2$+Se), E(SnS+Sn+Se), F(SnS+SnSe+Se), G(SnS+$SnSe_2$+Se), H(SnS+Se), I(SnS_2+Se)

Sample	2 Theta of (112) Peak (°)
A	27.21
B	27.21
C	27.21
D	27.21
E	27.38
F	27.43
G	27.43
H	27.43
I	27.71

Table S5. The positions of Raman peaks of A_1 mode of CAZTSSe for CAZTSSe thin films under the selenization conditions of A, B, C, D, E, F, G, H, I

Sample	A_1 mode Raman Shift (cm^{-1})
A	192.93
B	192.93
C	192.93
D	192.93
E	197.88
F	203.17
G	203.17
H	203.17
I	211.92

Table S6. Summary of the fitting results derived from EIS measurement

Device	R_s' (Ω)	R_{rec} (kΩ)
device-H	11.62	51.70
device-G	5.53	69.67
device-D	5.92	56.99

Table S7. Summary of TRPL fitting results of device-H, G and D

Device	$\tau_1\ (ns)$	A_1 (%)	$\tau_2\ (ns)$	A_2 (%)	$\tau_{avg}\ (ns)$
device-H	3.640	11.35	0.587	88.65	1.938
device-G	6.610	13.36	1.063	86.64	3.778
device-D	4.381	12.13	0.744	87.87	2.374

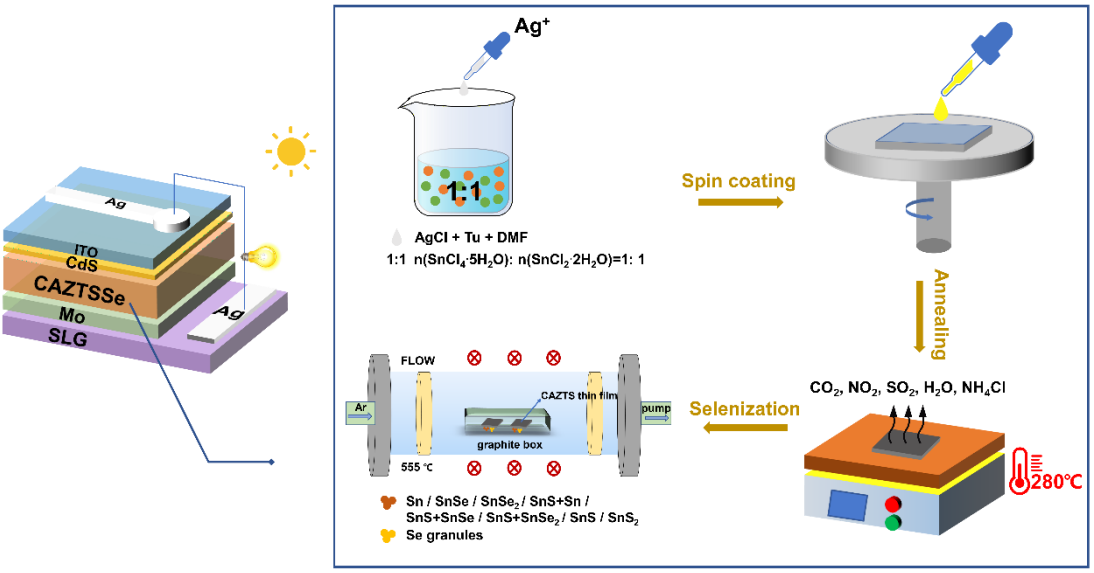

Figure S1. Schematic illustration of the fabrication process of CAZTSSe thin films.

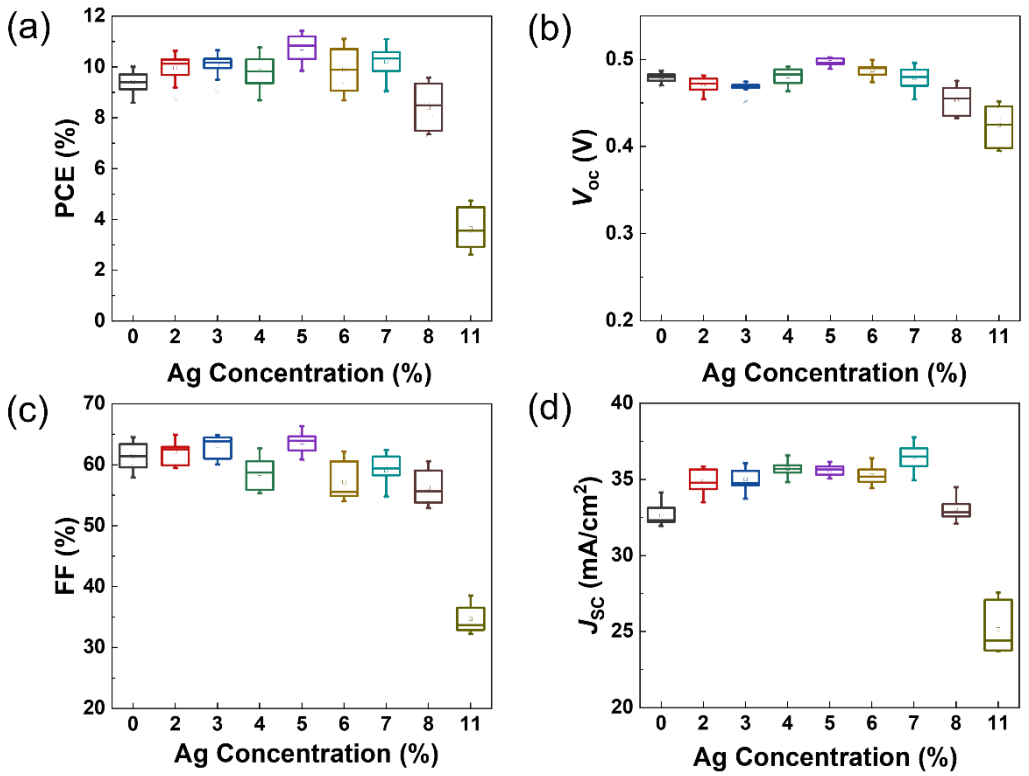

Figure S2. The statistical distribution of photovoltaic parameters including (a) PCE, (b) V_{OC}, (c) FF, and (d) J_{SC} of solar cells with different Ag ratios (0%, 2%, 3%, 4%, 5%, 6%, 7%, 8%, 11%).

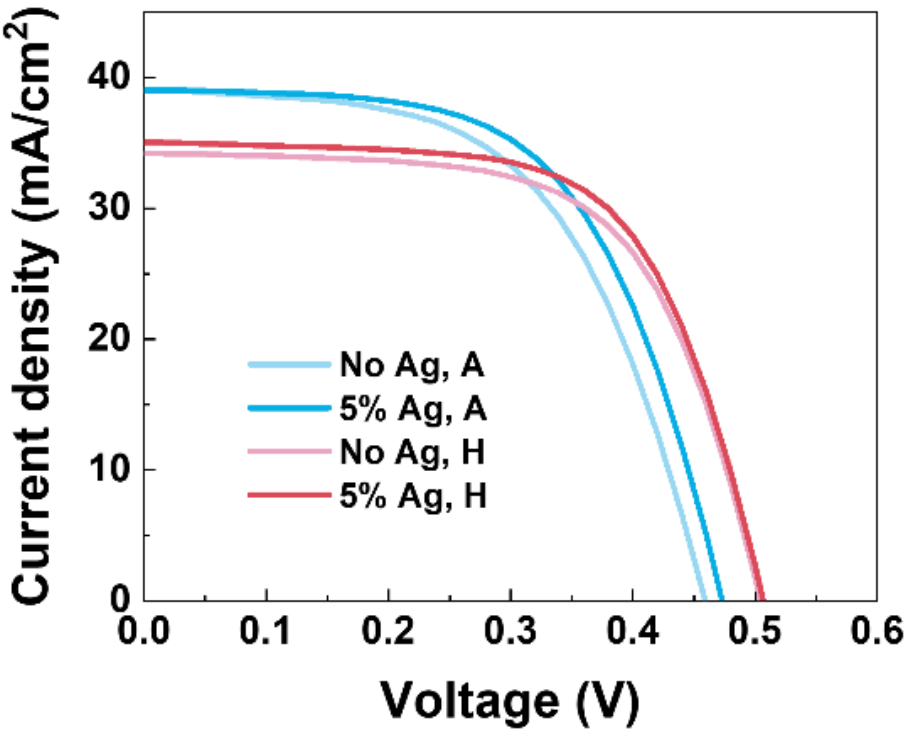

Figure S3. *J–V* curves of the champion solar cells without and with 5% Ag under the selenization conditions of A(Se) and H(SnS+Se).

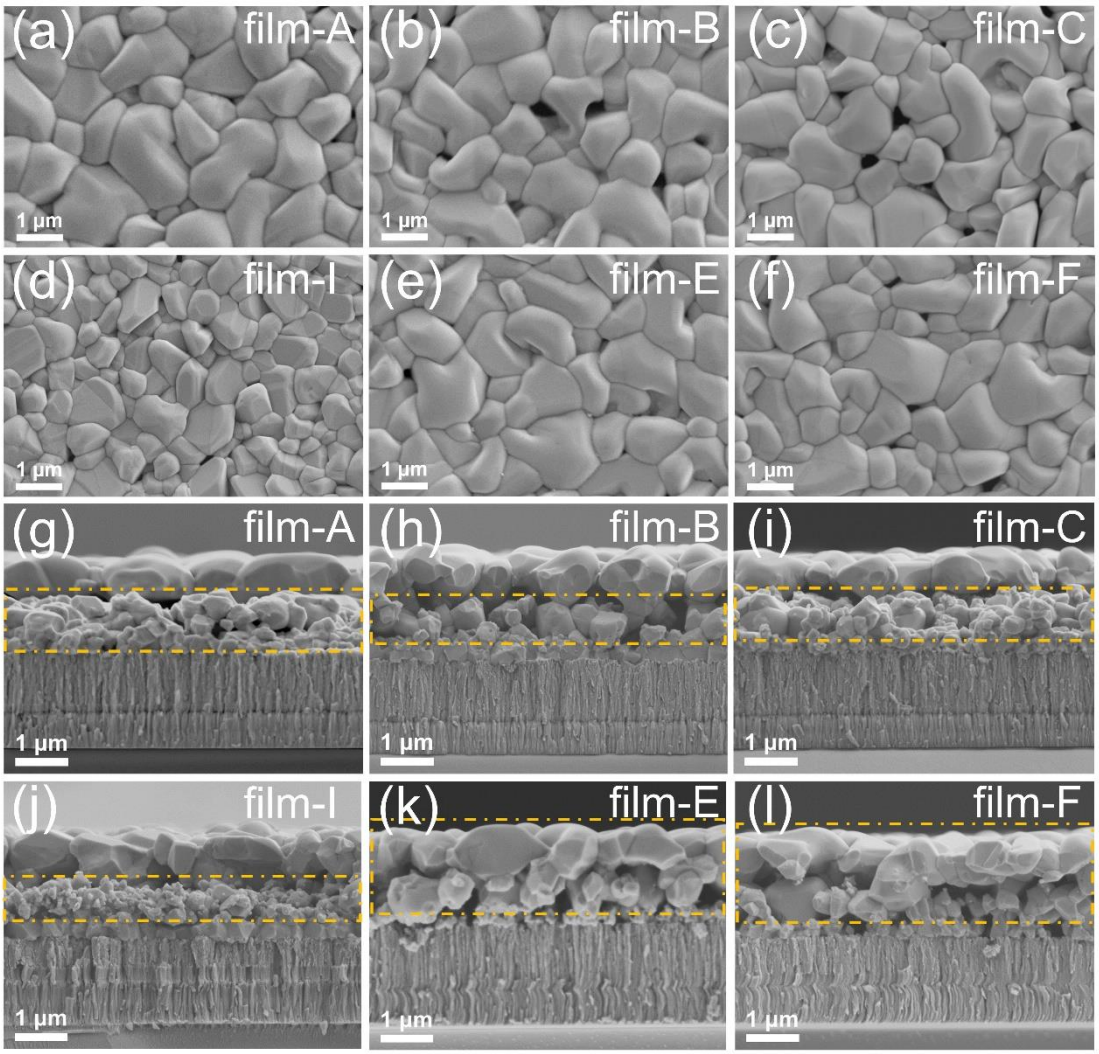

Figure S4. (a-f) The surface SEM images and (g-l) the cross-sectional images of CAZTSSe thin films under the selenization conditions of A(Se), B(Sn+Se), C(SnSe+Se), I(SnS_2+Se), E(SnS+Sn+Se), F(SnS+SnSe+Se).

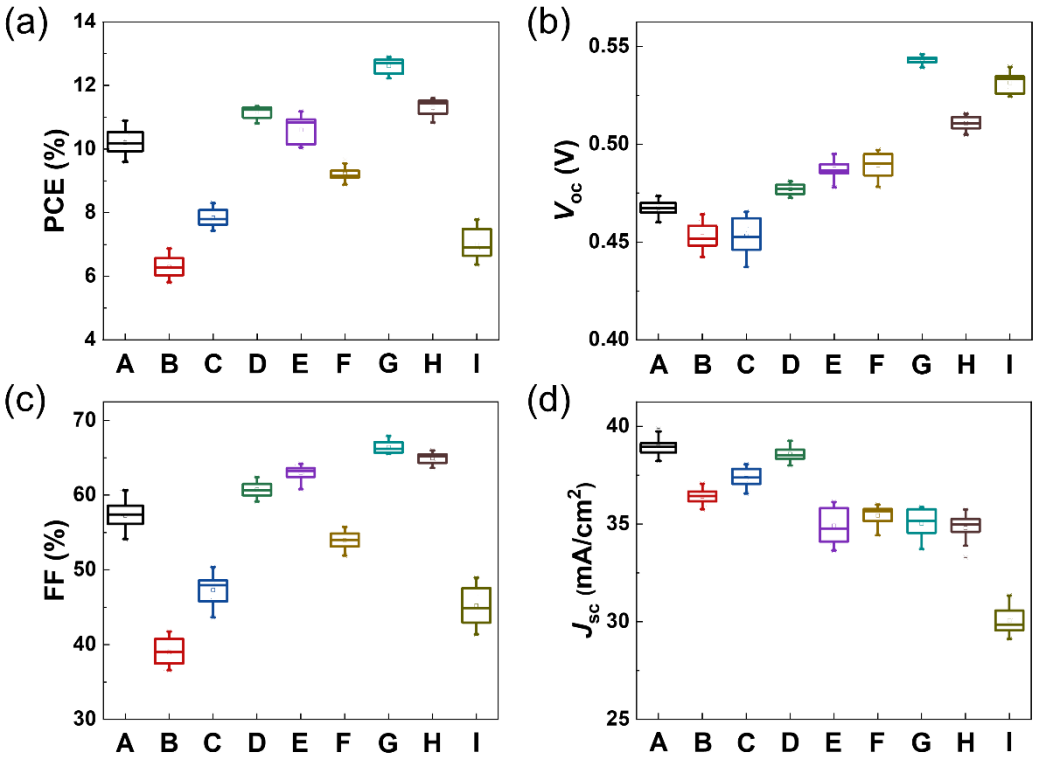

Figure S5. The statistical distribution of the devices' photovoltaic parameters including (a) PCE, (b) V_{OC}, (c) FF, and (d) J_{SC} under the selenization conditions of A(Se), B(Sn+Se), C(SnSe+Se), D($SnSe_2$+Se), E(SnS+Sn+Se), F(SnS+SnSe+Se), G(SnS+$SnSe_2$+Se), H(SnS+Se), I(SnS_2+Se).

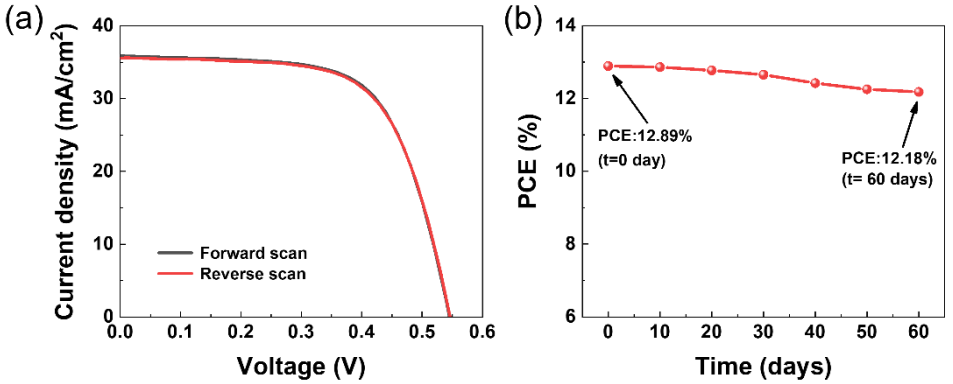

Figure S6. (a) *J-V* hysteresis behavior of the champion device; (b) The variation of PCE for the champion device during 60 days in ambient air without special encapsulation.

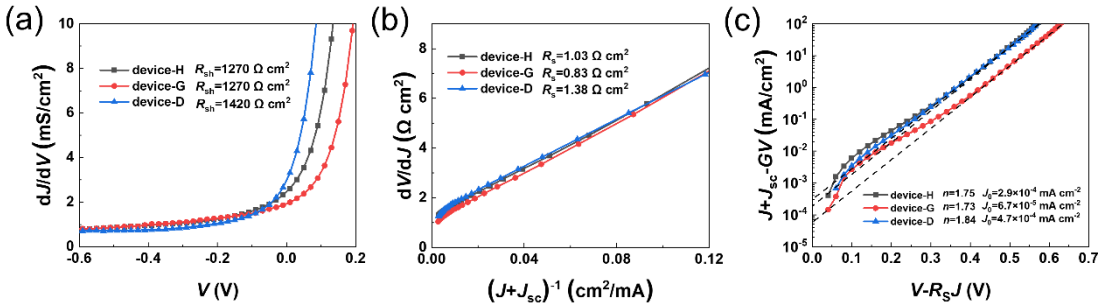

Figure S7. (a) Shunt resistance R_{sh}, (b) series resistance R_s, (c) diode ideality factor n and reverse saturation current density J_0 derived from J-V data via CurVA software.

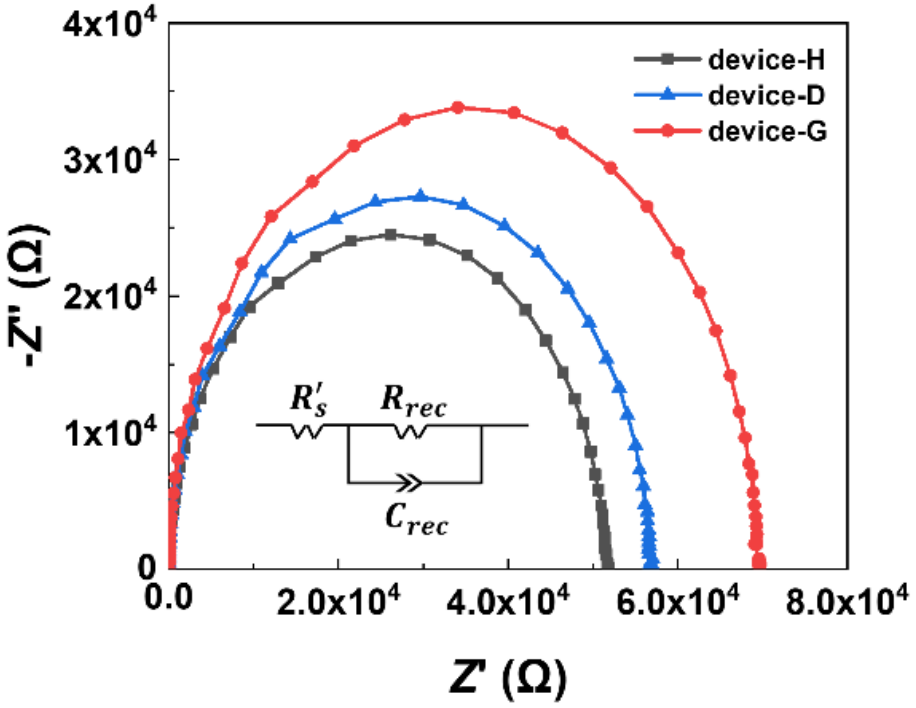

Figure S8. Electrochemical impedance spectra of device-H(SnS+Se), device-G(SnS+$SnSe_2$+Se) and device-D($SnSe_2$+Se).

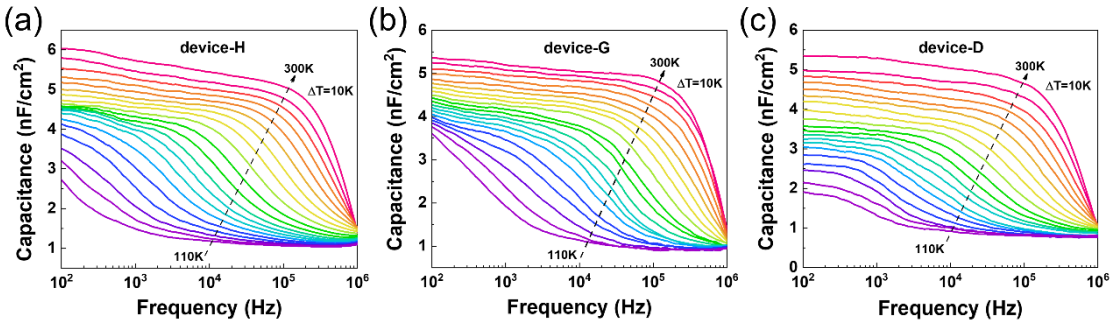

Figure S9. The admittance spectra of (a) device-H, (b) device-G and (c) device-D.

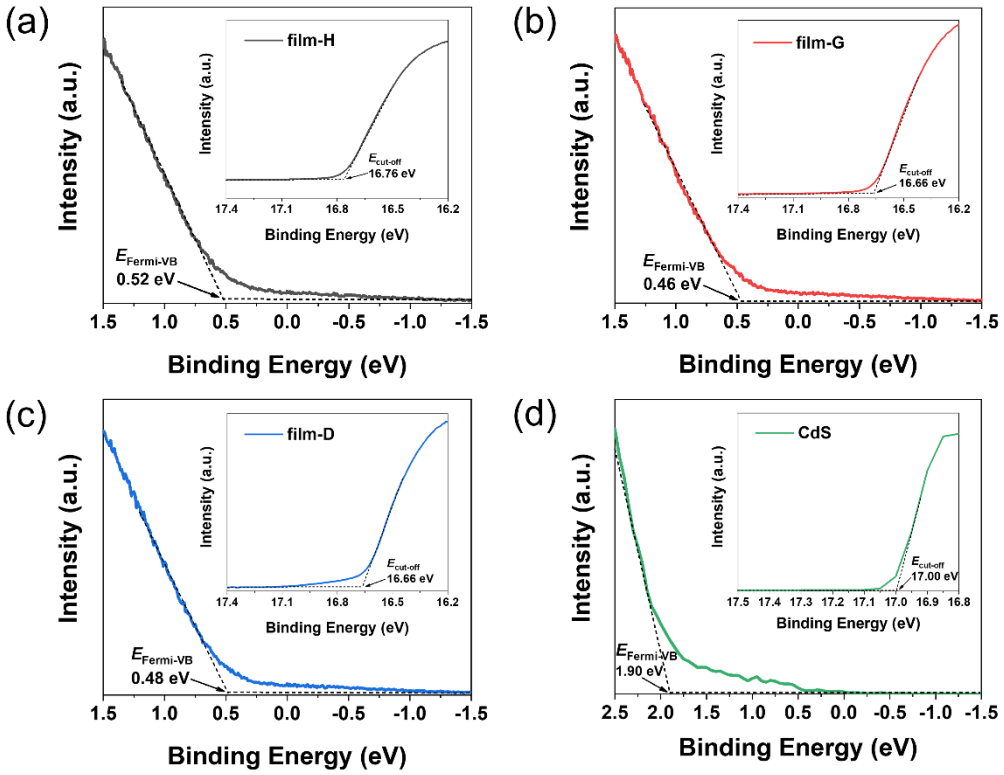

Figure S10. The energy of the Fermi level relative to the valence band ($E_{Fermi-VB}$) and the secondary electron cut-off edge ($E_{cut-off}$) derived from UPS of (a) film-H, (b) film-G, (c) film-D., and (d) buffer layer CdS. The plots of $E_{cut-off}$ were inset in (a), (b), (c) and (d).

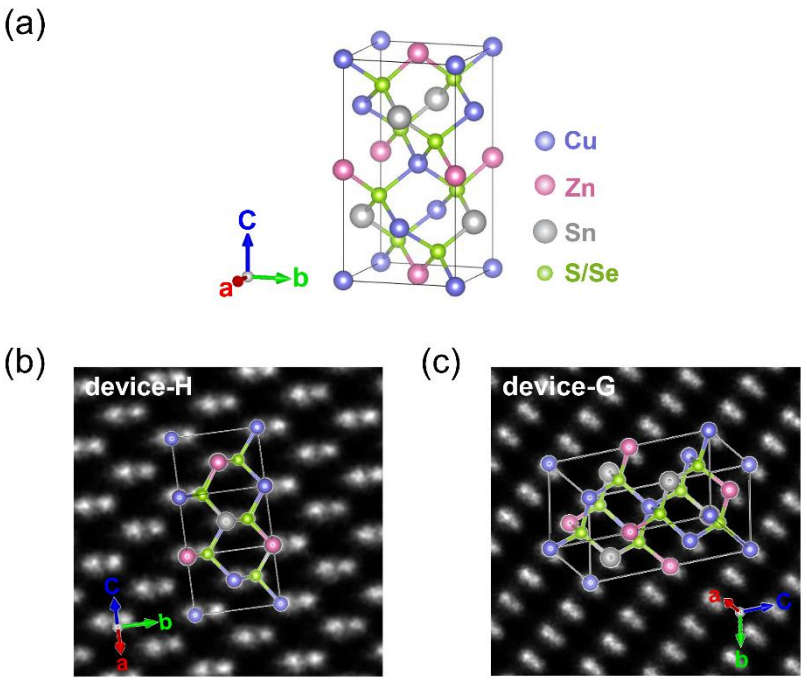

Figure S11. (a) The atomic structures of CZTSSe; The enlarged crystal lattice diagrams of (b) device-H, (c) device-G.

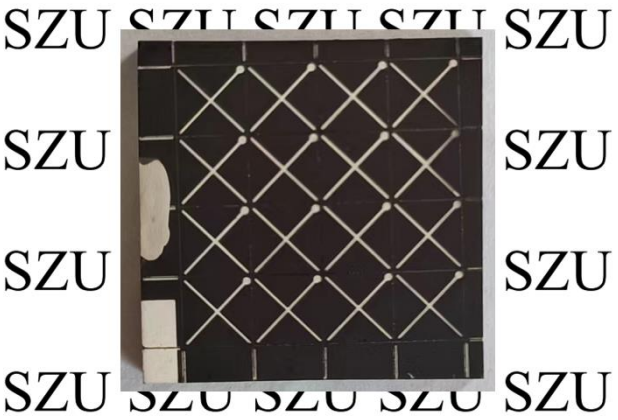

Figure S12. The photograph of the real device.

Supplementary Note 1. TRPL analysis

The TRPL decay curves were fitted by the bi-exponential function and the corresponding results were summarized in **Table S7**. The average minority carrier lifetime was calculated by the following equation:

$$\tau_{avg} = \frac{(A_1\tau_1^2+A_2\tau_2^2)}{A_1\tau_1+A_2\tau_2} \quad \text{(S1)}$$

where τ_1 and τ_2 are lifetime; A_1 and A_2 are the respective ratio of τ_1 and τ_2.

Supplementary Note 2. *C-V* and DLCP analysis

$N_{\text{C-V}}$ and the profiling depth X can be calculated according to the following equations:

$$N_{CV} = \frac{C^3}{qA^2\varepsilon_0\varepsilon_s}\left(\frac{dC}{dV}\right)^{-1} \quad \text{(S2)}$$

$$X_{CV} = \frac{A\varepsilon_0\varepsilon_s}{C} \quad \text{(S3)}$$

N_{DLCP} and the profiling depth X can be calculated according to the following equations:

$$N_{DL} = -\frac{1}{2q\varepsilon_0\varepsilon_s A^2}\frac{C_0^3}{C_1} \quad \text{(S4)}$$

$$X_{DL} = \frac{\varepsilon_0\varepsilon_s A}{C_0} \quad \text{(S5)}$$

where q is the electron charge, A is the total area of the solar cells, ε_0 is the vacuum permittivity, ε_s is the relative dielectric constant of CZTSSe, and C_0 and C_1 are two quadratic fitting parameters.

Supplementary Note 3. AS analysis

The admittance spectra were plotted by capacitance (C) vs. frequency (f), and the inflection frequency f_0 for each AS curve at different temperatures was determined by the maximum point of $-f\frac{dC}{df}$ vs. frequency. According to inflection angular frequency $\omega_0 = 2\pi f_0$, the Arrhenius plots of $ln\frac{\omega_0}{T^2}$ vs. $\frac{1000}{T}$ were obtained. The defect activation energy (E_a) and the attempt-to-escape frequency (ν_0) follow **Equation S6**:

$$\omega_0 = 2\pi\nu_0 T^2 \exp\left(\frac{-E_a}{\kappa T}\right) \quad \text{(S6)}$$

Where T is test temperature, after taking the log of this equation, the result is as follows:

$$\ln\left(\frac{\omega_0}{T^2}\right) = -\frac{E_a}{\kappa T} + \ln(2\pi\nu_0) \quad \text{(S7)}$$

E_a was derived from the slope of the Arrhenius plots, and ν_0 was extracted from the y-

axis intercept $\ln(2\pi\nu_0)$. Subsequently, to obtain energy distribution of defects, the energy as a function of angular frequency was presented in **Equation S8**:

$$E(\omega) = \kappa T ln\left(\frac{2\pi\nu_0 T^2}{\omega}\right) = \kappa T[\ln(2\pi\nu_0) - \ln\left(\frac{\omega}{T^2}\right)] \quad \text{(S8)}$$

And differential capacitance spectrum reflecting defect concentration at each temperature was superimposed, following **Equation S9**:

$$N_t[E(\omega)] = -\frac{V_{bi}}{qW\kappa T}\omega\frac{dC}{d\omega} \quad \text{(S9)}$$

where V_{bi} is built-in potential and W is the depletion region width of the junction, which are extracted from the plots of $\frac{1}{C^2}$ vs. V and N_{CV} vs. X in Capacitance-Voltage measurement. Normally, the values of E_a and $E(\omega)_0$ corresponding to the peak of N_t curve should be similar, which are the energy level of defects relative to the valence band maximum (VBM). The values of defect density (N_t) were obtained from the integral peak areas of N_t curve via Gaussian fitting.

Supplementary Note 4. UPS analysis

The work function (φ) can be calculated by the following equation:

$$\varphi = h\nu - E_{cut\ off} \quad \text{(S10)}$$

Where $h\nu$ is 21.22 eV (He I source) here.